

***ArrayTac*: A tactile display for simultaneous rendering of shape, stiffness and friction**

Tianhai Liang¹, Shiyi Guo¹, Baiye Cheng²,

Zhengrong Xue¹, Han Zhang¹, Huazhe Xu^{1*}

¹IIS, Tsinghua University, Beijing & 100084, China.

²EIC, Huazhong University of Science and Technology, Wuhan & 430074, China.

*Corresponding author. Email: huazhe_xu@mail.tsinghua.edu.cn

Human-computer interaction in the visual and auditory domains has achieved considerable maturity, yet machine-to-human tactile feedback remains underdeveloped. Existing tactile displays struggle to simultaneously render multiple tactile dimensions, such as shape, stiffness, and friction, which limits the realism of haptic simulation. Here, we present ArrayTac, a piezoelectric-driven tactile display capable of simultaneously rendering shape, stiffness, and friction to reproduce realistic haptic signals. The system comprises a 4×4 array of 16 actuator units, each employing a three-stage micro-lever mechanism to amplify the micrometer-scale displacement of the piezoelectric element, with Hall sensor-based closed-loop control at the end effector to enhance response speed and precision. We further implement two end-to-end pipelines: 1) a vision-to-touch framework that converts visual inputs into tactile signals using multimodal foundation models, and 2) a real-time tele-palpatation system operating over distances of several thousand kilometers. In user studies, first-time participants accurately identify object shapes and physical properties with high success rates. In a tele-palpatation experiment over 1,000 km, untrained volunteers correctly identified both the number and

type of tumors in a breast phantom with 100% accuracy and precisely localized their positions. The system pioneers a new pathway for high-fidelity haptic feedback by introducing the unprecedented capability to simultaneously render an object's shape, stiffness, and friction, delivering a holistic tactile experience that was previously unattainable.

Introduction

Haptic perception plays a pivotal role in human interaction with the physical world. Through the coordinated action of diverse mechanoreceptors embedded in the skin, humans can accurately discern an object's shape, stiffness, and friction (1–4). This capability is indispensable not only for everyday manipulation and material identification, but also for domains that demand high precision and intuitive feedback, such as medical diagnosis, precision manufacturing, and remote operation (5–7). While the visual and auditory channels underpinning virtual reality (VR) and teleoperation are highly mature, haptic technology remains a critical bottleneck for truly immersive experiences (1, 8). The most critical gap lies in the simultaneous rendering of multiple tactile modalities, a limitation that directly constrains the realism of immersive haptic experiences (1, 5, 7, 8).

An ideal haptic display should provide high-refresh-rate rendering across multiple tactile dimensions—particularly shape, stiffness, and friction—which are essential for humans to perceive and interpret the surface properties of objects (9). Researchers have explored a wide spectrum of haptic display actuation strategies, each offering distinct advantages and trade-offs.

Mechanically driven systems employ motors, cams, or linkage mechanisms to directly displace the contact interface, enabling high output force and displacement with an intuitive structure. They usually can only display the shape dimension and suffer from limited response speed with challenging miniaturization (10–12). Electromagnetic actuators generate displacement through interactions between coils and permanent magnets, typically rendering shape dimension only through vibration-based cues. Although they offer advantages in frequency response, their scalability is limited by magnetic crosstalk between units, complex mechanical architectures, and heat generation (13–16). Ultrasonic displays focus acoustic pressure or air vibrations onto the skin to create non-contact

forces, enabling contactless interactions, yet their force output is modest and spatial resolution is limited (17, 18). The electrical stimulation method directly uses specially modulated electric current to stimulate the skin, thereby producing a variety of tactile sensations, but the sensations it brings are often unpleasant, and the display performance is greatly affected by the surface condition of the skin (19–22). Some special materials can also be used to make tactile displays, such as organic polymer and memory alloys, but low bandwidth and harsh usage conditions, like high voltage, are often their bottlenecks (23–27). Pneumatic and hydraulic systems modulate pressure using miniature pumps or fluidic channels, achieving compliance and safety well-suited to wearable haptic gloves, but their performance is constrained by cumbersome tubing layouts and latency in actuation (28–30). Some special designs can make the hydraulic system achieve high bandwidth at about 200 Hz, but its maximum displacement is only about 100 μm (31). In comparison, piezoelectric actuators—operating via the inverse piezoelectric effect—can achieve microscale displacements within microseconds (32), combining compact form factors, high frequency response, and scalability, making them strong candidates for high-resolution haptic arrays (33–40).

Despite these advances, current haptic display technologies face fundamental limitations. Most systems can only reproduce a single tactile attribute—such as shape or friction—at a time, lacking the ability to render multiple tactile dimensions simultaneously on a single platform, thereby diminishing perceptual richness and realism (1, 5, 8). The representation of stiffness remains particularly underdeveloped; only a handful of devices can display stiffness, and even then, they typically operate at a single contact point, making high-resolution stiffness mapping infeasible (23, 41–43). In terms of perceptual encoding, some systems adopt mappings that deviate from natural tactile logic—for example, representing surface height through vibration frequency—forcing users to undergo additional adaptation training before effective use (13, 14, 33, 39). Moreover, frequency response performance is generally limited; pneumatic systems, in particular, often have cutoff frequencies well below the thresholds required for high-fidelity tactile rendering, restricting refresh rates and dynamic realism (28). Compounding these challenges, few of them are continuously adjustable for displaying shape information, and most devices operate in an open-loop mode without real-time feedback control, making them vulnerable to external disturbances (e.g., variations in fingertip pressure) and leading to unstable or inaccurate tactile representation (13–21, 23–31, 33–40).

To address these challenges, we present ArrayTac, an array-based multidimensional tactile

texture display actuated by piezoelectric actuators with a multi-stage micro-lever amplification mechanism. The device can naturally and simultaneously render shape, stiffness, and friction on a unified platform with continuously tunable parameters. Each display unit integrates an independent Hall effect sensor (44) at the end-effector to measure displacement, enabling closed-loop control that actively compensates for external perturbations while extending control bandwidth, thereby markedly improving response speed and display accuracy. With the addition of a sliding platform, ArrayTac enables active sliding exploration, allowing users to achieve high spatial-resolution perception. In addition, we developed a stiffness control algorithm that emulates the mechanical behavior of soft materials, enabling independent modulation of stiffness at each display unit. Building on this hardware, we developed a complete tactile rendering pipeline, including real-time hand tracking and real-time tactile display. This architecture supports complex, application-relevant tactile interaction tasks, ranging from touching virtual items to remote medical palpation. Our system serves as a pivotal interface for the extension of human perception, transforming how we interact with the digital world by restoring high-fidelity, multidimensional physical feedback. This advancement lays the groundwork for critical breakthroughs in tele-interventions, accessible technology for the blind, and fully immersive virtual environments.

Results

ArrayTac pioneers a new way for high-fidelity haptics by simultaneously rendering shape, stiffness, and friction on a single, unified platform. Through rigorous psychophysical evaluations, we demonstrate the device’s exceptional ability to deliver intuitive, multidimensional tactile feedback. We demonstrate the system’s potential applications through two end-to-end frameworks. First, the Tac-Anything pipeline leverages foundation models to automatically extract and render tactile semantics directly from 2D images. Second, our Tele-Touch framework enables high-fidelity remote perception. We highlight this capability with a groundbreaking real-world clinical demonstration: a cross-city breast tumor palpation task. In this cross-city experiment, completely untrained volunteers remotely palpated a professional medical silicone phantom from over 1000 km away using ArrayTac. They successfully localized hidden tumors and achieved a remarkable 100% accuracy in distinguishing between malignant and benign tumors.

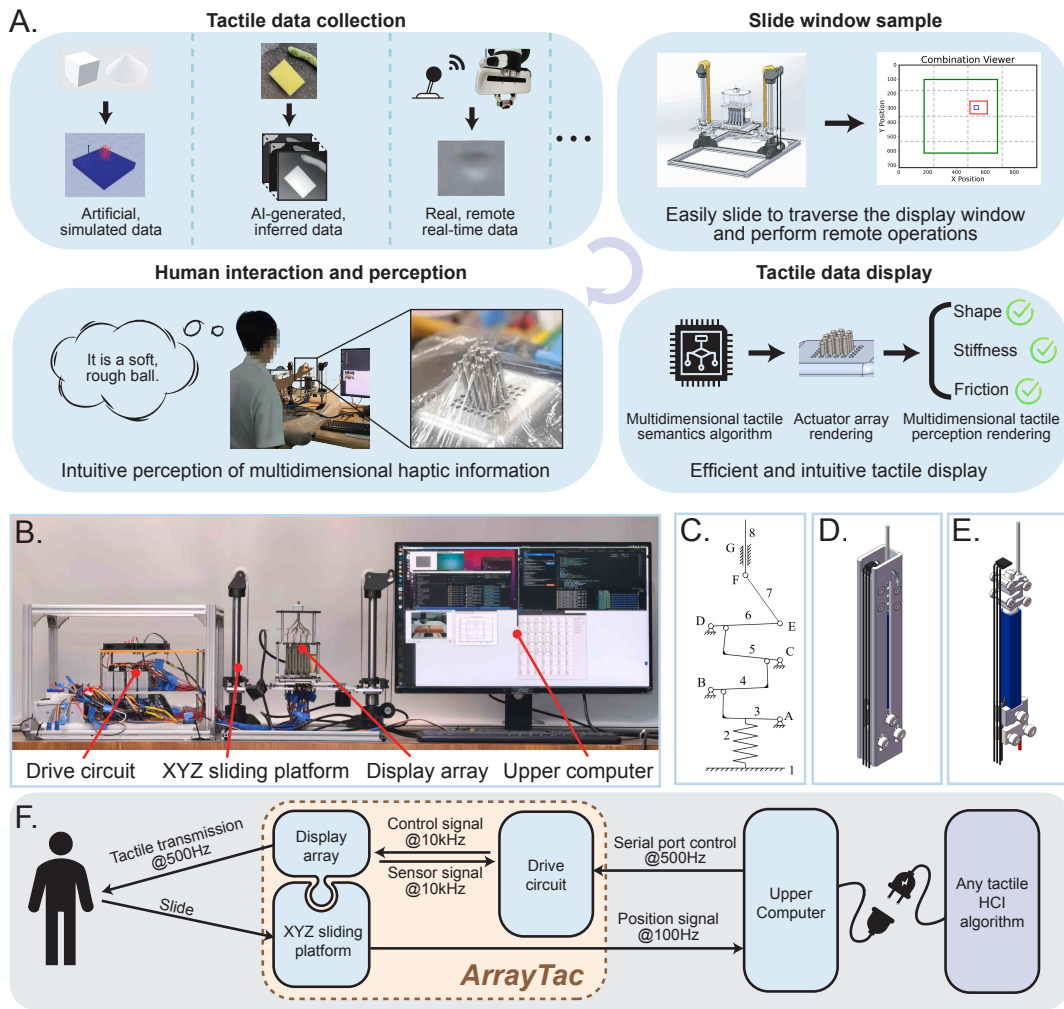


Figure 1: The ArrayTac system: architecture, hardware, and control pipeline. (A) This panel illustrates the system workflow, showing the data pipeline from multi-source tactile data collection to haptic rendering. (B) This photograph shows the complete experimental setup with its main hardware components. (C) Schematic diagram of a single actuator unit mechanism. (D) An external view of a fully assembled actuator unit. (E) An internal perspective view of an actuator unit. (F) This is the information flow block diagram, which details the information flow and communication between components. The diagram shows user input from the XYZ sliding platform, high-frequency communication between the display array and drive circuit (10 kHz), and communication with the upper computer. This system can be seamlessly integrated with any Human-Computer Interaction (HCI) algorithm in a plug-and-play manner.

A High-Performance Tactile Display Architecture

Our tactile display system is engineered as a comprehensive haptic solution, capable of simultaneously rendering an object's shape, stiffness, and friction with high fidelity. Its architecture, illustrated in Fig. 1A, is designed first to acquire tactile data from diverse sources—including physical simulations, AI-based inference from images, and real-time remote sensors. This data is then sampled by the user in real time through a “sliding window” to select a region of interest. The sampled information is processed by a multidimensional tactile semantics algorithm that drives the actuator array to render the corresponding shape, stiffness, and friction. This tactile display hardware is realized by three core subsystems: a high-displacement 4×4 actuator array, a custom high-performance drive circuit, and a zero-gravity sliding platform, with the complete experimental setup shown in Fig. 1B. This integrated design achieves a stable array refresh rate exceeding 500 Hz, enabling the real-time display of dynamic tactile sensations.

The core of the system is the array of 16 individually addressable actuator units. As shown in Fig. 1C, each unit employs a novel three-stage micro-lever mechanism that amplifies the initial $40 \mu\text{m}$ displacement from a piezoelectric ceramic element by a factor of 125, resulting in a substantial vertical displacement of up to 5 mm. To enable precise closed-loop control, each actuator incorporates a Hall sensor-based position sensing module. The complete assembly of the unit is shown in Fig. 1D, while its internal structure is detailed in Fig. 1E. This entire array is mounted on an XYZ sliding platform to extend the interactive workspace (Fig. 1B); this platform is gravity-compensated for effortless manipulation and uses rotary encoders for real-time position tracking. The actuator array is powered by a custom-designed drive circuit engineered for the precise and rapid control required for high-fidelity haptics. Detailed schematics and design principles are provided in the Materials and Methods section, Tactile Display System Design and Fabrication part. The overall information flow architecture is illustrated in Fig. 1F: the entire system can be seamlessly integrated with any HCI algorithm in a plug-and-play manner, enabling tactile interaction with a stable refresh rate of over 500 Hz.

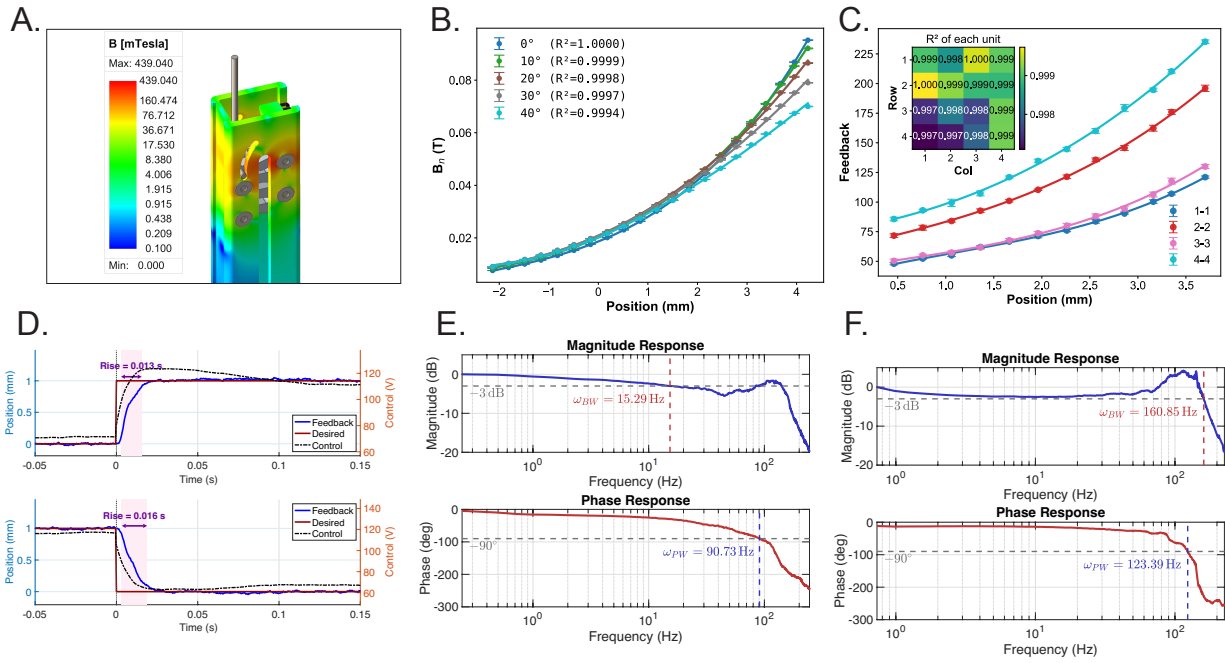


Figure 2: Unit control method and performance. (A) Electromagnetic field simulation process performed using Ansys EDT. (B) Simulated normal magnetic flux density (B_n) detected by the Hall sensor as a function of end-effector position at various sensor installation angles (0° to 40°). The solid lines are cubic polynomial fits to the data, with the coefficient of determination (R^2) for each fit shown in the legend. The consistently high R^2 values demonstrate the model's robustness against potential assembly misalignments of the sensor ($n = 5$). (C) Experimentally measured relationship between Hall sensor feedback and end-effector displacement for each unit. For clarity, only diagonal units are plotted, while the heatmap reports the coefficient of determination (R^2) for all 16 units ($n = 3$). For (B) and (C), data points are shown as mean \pm s.d., where n represents the number of samples. (D) Step response of a single display unit. (E) Bode plot of a single display unit under open-loop control. (F) Bode plot of a single display unit under PID closed-loop control. For (E) and (F), ω_{BW} denotes the -3 dB magnitude frequency and ω_{PW} denotes the -90° phase-lag frequency.

Intuitive Shape Rendering Enabled by Closed-Loop Control

A grand challenge in haptics is to create displays that render 3D shapes realistically enough for intuitive interpretation without prior training. Most existing systems fall short because they cannot produce continuously adjustable height profiles, instead relying on binary height outputs or indirect cues such as vibration. Their open-loop designs are also vulnerable to disturbances such as finger pressure, resulting in unstable or distorted feedback. Consequently, users typically require extensive training to interpret rendered shapes. Here, we aim to overcome this limitation by developing a high-fidelity haptic system that enables zero-shot identification, allowing naive users to recognize complex 3D shapes through touch alone.

To achieve this, we developed a high-fidelity shape rendering engine based on closed-loop position control. Each of the 16 actuator units integrates a Hall effect sensor for real-time end-effector feedback. A PID-controlled loop enables continuously adjustable height profiles, actively rejects disturbances, and precisely tracks target geometries. To validate the sensor-to-displacement model, we conducted rigorous experiments both in simulation and on the physical hardware. In simulation, we first modeled the sensor’s inherently nonlinear response using Ansys EDT software (Fig. 2A) and confirmed that a cubic polynomial fit is both highly accurate ($R^2 > 0.999$) and robust to potential assembly variations (Fig. 2B). Subsequently, we validated this model on all 16 fabricated actuators, confirming a highly consistent and accurate fit ($R^2 > 0.997$) in practice (Fig. 2C). Furthermore, we comprehensively characterized the dynamic performance of the closed-loop system. This involved analyzing its step response (Fig. 2D) and comparing the open-loop (Fig. 2E) versus closed-loop (Fig. 2F) frequency responses. This analysis demonstrated a more than eight-fold improvement in control bandwidth, from 15.29 Hz to 123.39 Hz. The detailed experimental procedures for this validation are presented in the Materials and Methods section, High-Fidelity Shape Rendering System: Design and Validation part.

To assess whether high-fidelity rendering supports intuitive perception, we conducted a three-part psychophysical study with 22 naive volunteers without prior haptics experience. Participants reported no tactile impairments and provided informed consent. Six geometric models (Fig. 3A) were designed in SolidWorks and processed using V-HACD to generate convex hulls for stable simulation. During trials, a PyBullet simulator sampled surface heights according to the real-time

finger position on the sliding platform and transmitted the data to the actuator array. To isolate shape perception, the normalized stiffness parameter was fixed ($k = 1$), and friction rendering was disabled.

Performance was quantified as follows: zero-shot identification (“Task 1”) was scored on a 0-5 scale based on descriptive accuracy (5 for perfect identification, 4 for most features, 3 for some features, 2 for limited information, 1 for mostly incorrect, and 0 for complete failure). Meanwhile, forced-choice classification tasks (“Tasks 2” and “Task 3”) were evaluated using confusion matrices.

Task 1: Zero-Shot Identification In the first phase, we assessed the ability of untrained users to identify the six shapes through touch alone without any cues or prior exposure. The results (Fig. 3B) confirm a high level of intuitive recognition. For simple objects like the hemisphere, cone and cube, participants achieved near-perfect identification (median score = 5). For more complex shapes like the bow-shaped prism and semi-ellipsoid, users consistently described key geometric features such as curvature and sharp edges (median score = 4), with only the triangular prism proving more challenging (median score = 3), likely due to the array’s spatial resolution limits.

Task 2: Forced-Choice Classification without Training In the second phase, participants were shown images of all six candidate objects, then asked to identify a randomly rendered shape from that known set. The resulting confusion matrix (Fig. 3C) revealed a high level of performance, with accuracies exceeding 72% across all object categories. Notably, misclassifications were logical, occurring between shapes with similar tactile features, which confirms that the device conveys meaningful and distinguishable haptic information.

Task 3: Forced-Choice Classification with Training The final phase measured performance improvement following a brief training session where participants could simultaneously see and feel each object through the device. It is worth noting that all existing tactile display systems currently require this type of procedure for participants to successfully recognize object shapes (12, 14, 15, 28, 29, 39, 42, 45). However, it is the easiest task in our experimental setting. The results, shown in the confusion matrix in Fig. 3D, demonstrated a marked and significant increase in accuracy, with all shapes achieving recognition rates over 86%. This demonstrates that the tactile feedback is not only intuitive but also highly learnable.

Taken together, these findings establish the device’s superior shape-rendering capabilities. The success in the zero-shot identification task is particularly significant. To our knowledge, this is the first fingertip tactile display demonstrated to enable naive users, without any prior experience or training, to correctly identify complex three-dimensional shapes from haptic feedback alone.

Rendering and Perception of Nonlinear Stiffness

Accurately rendering material stiffness is essential for haptic realism and requires reproducing nonlinear force-displacement behavior. This is especially critical for soft objects like biological tissue or silicone, which exhibit a complex, biphasic response to indentation. This signature tactile response involves an initial phase of high stiffness, followed by a distinct yielding or buckling phase once a certain force threshold is met. Linear models assuming constant stiffness cannot reproduce this behavior and therefore produce unrealistic tactile sensations. To address this, we developed a control strategy that reproduces this nonlinear response.

The method implements a two-stage control law: PID closed-loop control for the high-stiffness region and a feedforward penalty term for the yielding phase. Simulation and hardware experiments indicate that a quadratic penalty achieves the best trade-off between realism and stability. To ground the key normalized stiffness parameter k in a standardized metric, we established a calibration procedure mapping it to the Shore 00 hardness scale, yielding a robust near-linear relationship. Full derivations and calibration details are provided in the Materials and Methods section, Rendering Nonlinear Stiffness via Feedforward Penalty Control part.

We conducted a two-part psychophysical study to evaluate whether users could reliably perceive the rendered stiffness levels. Based on our analysis, five perceptually distinct stiffness levels were generated by evenly dividing the normalized stiffness parameter k within the effective range of 0.5 to 1.0, corresponding to a progression from the softest to the hardest setting. To isolate stiffness perception, all actuators were fixed at a 3 mm displacement to form a flat platform, and friction rendering was disabled.

Task 1: Pairwise Discrimination In the first phase, we assessed the relative discriminability of the five stiffness levels by asking participants to identify the stiffer of two randomly presented stimuli. The results, visualized in the preference heatmap (Fig. 3E), indicate excellent discrimination

capability. The accuracy for distinguishing between adjacent stiffness levels exceeded 86%, and for non-adjacent levels, it reached 100%, confirming that each level is clearly perceptible.

Task 2: Absolute Identification In the second phase, we evaluated the absolute identification of the rendered stiffness. After a brief familiarization period with all five levels, participants were asked to classify a single, randomly presented stimulus. The resulting confusion matrix (Fig. 3F) reveals a high classification accuracy of over 74% across all conditions. This demonstrates that the rendered stiffness levels are not only distinguishable but also possess unique and memorable tactile signatures.

Collectively, these experiments confirm that the system can reliably render and convey stiffness information. Users can not only discern subtle differences between stiffness levels but can also identify specific levels with high precision. This capability to generate at least five clearly distinguishable stiffness grades is crucial for rendering realistic virtual objects.

Rendering and Perception of Friction via Vibrotactile Cues

Human friction perception depends not only on tangential resistance but also on high-frequency vibrations generated during sliding (46). Psychophysical studies identify these vibrotactile cues as primary determinants of perceived texture and friction (47). Inspired by these findings, our system focuses on recreating these critical vibrations to elicit a realistic and compelling frictional experience.

Each actuator produces independent sinusoidal vibrations superimposed on shape-rendering displacement, with amplitudes up to 5 mm and frequencies from 0 to 512 Hz, within reported perceptual ranges for texture exploration (47, 48). To enhance perceptual salience and simplify control, we linearly couple the vibration amplitude, frequency, and PID gain, so that they increase proportionally with commanded friction. This coordinated modulation produces a stronger sensation of increasing frictional force, governed by a single normalized parameter $f \in [0, 1]$.

To validate the perceptual effectiveness of this rendering method, we conducted a two-part psychophysical study with 22 volunteers. For the study, the normalized friction command f was mapped to a perceptually salient frequency range of 0 to 200 Hz, which was then evenly divided into five distinct levels for testing. To isolate the perception of friction, all other tactile cues were

neutralized: the device was maintained in a flat platform configuration (all actuators at 3 mm displacement), and the stiffness was fixed at its maximum value ($k = 1$).

Task 1: Pairwise Discrimination In the first task, participants were presented with random pairs of stimuli and asked to identify which felt “rougher.” The results, visualized in the preference heatmap (Fig. 3G), were definitive: discrimination accuracy across all possible pairwise combinations was 100%. This perfect score indicates that the five rendered friction levels are exceptionally distinct and easily discernible.

Task 2: Absolute Identification In the second task, we evaluated participants’ ability to identify the absolute friction levels. After a brief familiarization period, they were asked to classify a single, randomly presented stimulus level. The results demonstrate strong discriminability, with the confusion matrix (Fig. 3H) indicating classification accuracies exceeding 87% across all levels. This demonstrates that each rendered friction level possesses a unique and memorable tactile signature that can be reliably identified.

In summary, these results provide strong evidence that rendering friction via modulated vibrotactile cues is a highly effective and perceptually robust method. Users can flawlessly differentiate between friction levels and identify them with exceptional accuracy, confirming the device’s capability to reproduce a controllable and diverse range of surface textures.

Tac-Anything Framework and Rendering Experiments

A key limitation of traditional haptic rendering is its reliance on inefficient, per-object measurement and calibration. Recent advances in Vision-Language Models (VLMs), however, enable a more scalable approach: inferring tactile properties such as stiffness and friction from a single image through few-shot learning. Using this capability, we introduce Tac-Anything, a novel framework that extracts these multidimensional tactile semantics and displays them from only an RGB image. The complete pipeline is illustrated in Fig. 4A, with a detailed description provided in the Materials and Methods section, Tac-Anything Framework part.

To validate the effectiveness of our framework, we designed a scene reconstruction experiment. We selected eight common household objects with diverse tactile properties (Fig. 4B) and arranged

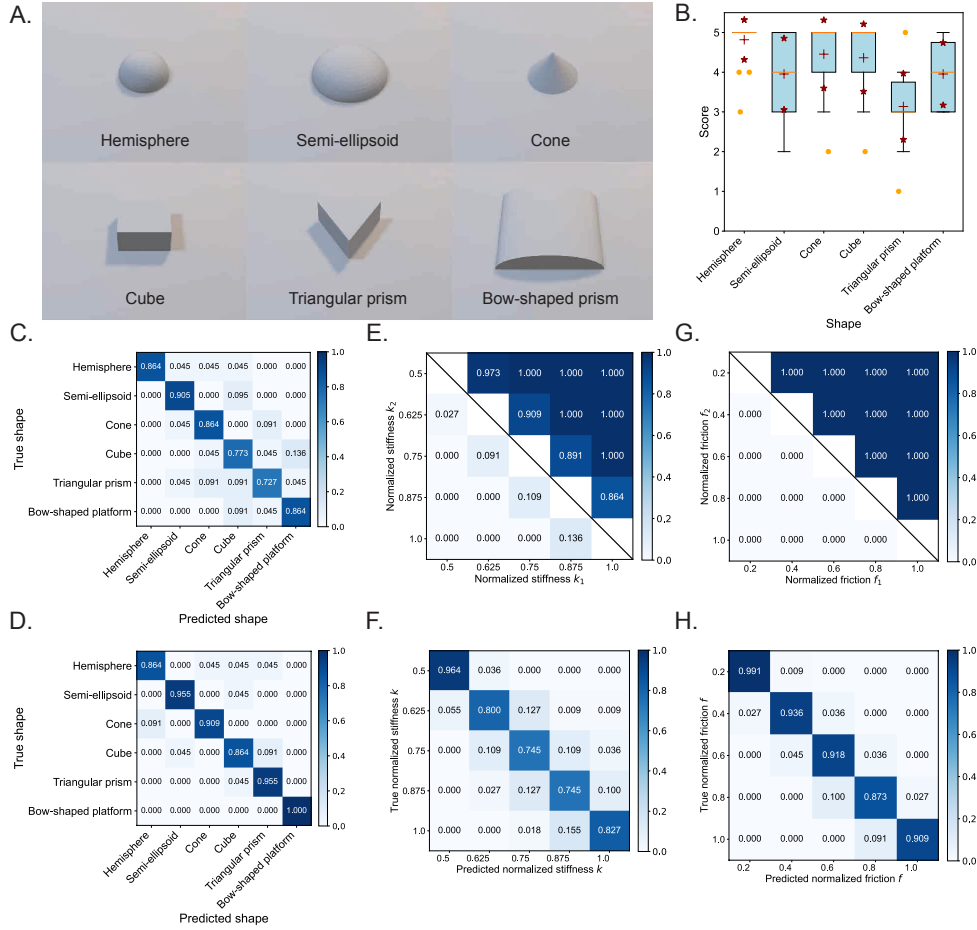


Figure 3: Volunteer experiments on shape, stiffness, and friction perception. (A) 3D models used in the shape discrimination experiment. (B) Zero-shot performance scores of volunteers during their first use of the device without any prior training ($n = 22$). In the box plot of (B), the central mark indicates the median, and the red ‘+’ symbol indicates the mean. The bottom and top edges of the box represent the 25th and 75th percentiles, respectively. The whiskers extend to the maximum and minimum values excluding the outliers, which are plotted individually using the orange points. (C) Confusion matrix of shape identification when volunteers were provided only with the list of candidate options ($n = 22$). (D) Confusion matrix of shape identification after volunteers completed training ($n = 22$). (E) Pairwise preference heatmap for stiffness discrimination, illustrating the proportion of trials where k_1 was judged stiffer than k_2 ($n=22 \times 5$). (F) Confusion matrix of classification across different stiffness levels ($n=22 \times 5$). (G) Pairwise preference heatmap for friction discrimination, illustrating the proportion of trials where f_1 was judged rougher than f_2 ($n=22 \times 5$). (H) Confusion matrix of classification across different friction levels ($n=22 \times 5$).

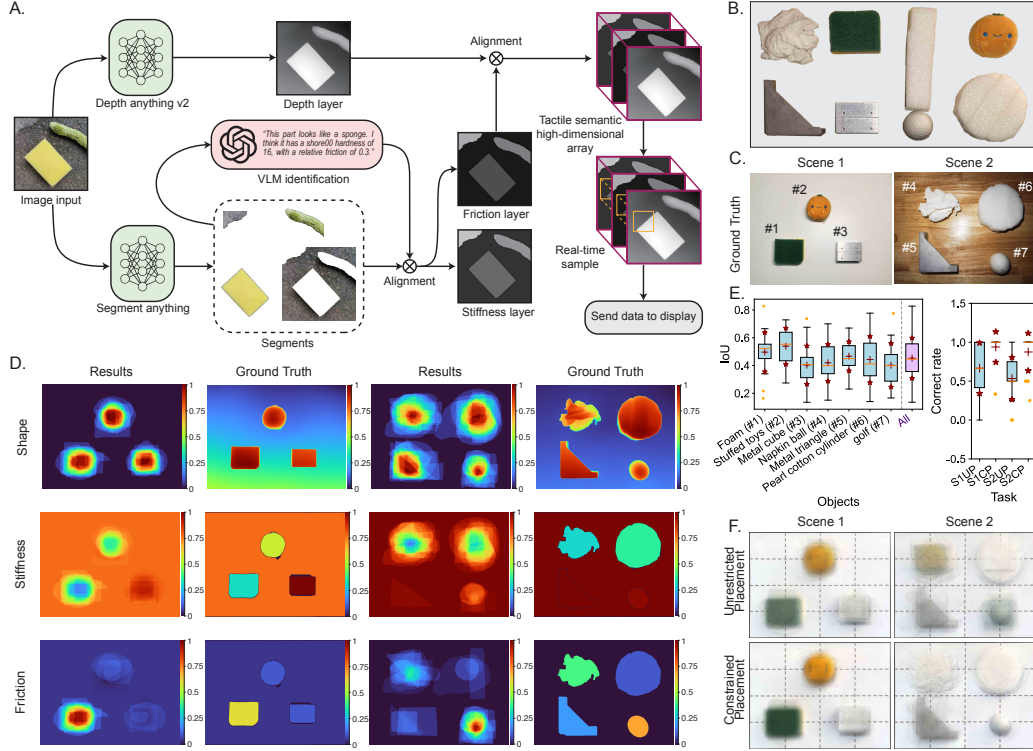


Figure 4: The Tac-Anything framework: architecture, experimental validation, and performance. (A) An overview of the Tac-Anything framework, which extracts and renders multidimensional tactile semantics (shape, stiffness, and friction) from a single RGB image. (B) The eight real-world objects with diverse tactile properties used in the user study. (C) The two photographic scenes used as the ground truth. (D) Average Sketching maps of the Haptic Scene Sketching task ($n=22$). Participant sketches, including their normalized annotations for shape, stiffness, and friction, are compared against the ground truth tactile maps for both scenes. (E) Quantitative analysis of user performance presented as box plots ($n = 22$). The left plot shows the Intersection over Union (IoU) for the Haptic Scene Sketching task for each object and the result for all objects ('all'). The right plot shows the object placement accuracy for the Object Identification and Placement task across four conditions: Scene 1, Unrestricted Placement (S1UP); Scene 1, Constrained Placement (S1CP); Scene 2, Unrestricted Placement (S2UP); and Scene 2, Constrained Placement (S2CP). (F) Average placement maps for the Object Identification and Placement task ($n = 22$), aggregating the final objects and positions chosen by all participants.

them into two distinct tabletop scenes (Fig. 4C). Photographs of these scenes were processed by the Tac-Anything framework to generate the tactile semantic information, which was then sent to the ArrayTac. Participants then performed two tasks to evaluate this framework:

Task 1: Haptic Scene Sketching In this task, participants explored the tactile scene and were asked to sketch their perception of the layout. They used their own notation to annotate the shape, stiffness, and friction properties of each region. We digitized the collected drawings and normalized the stiffness and friction values to a range of $[0, 1]$ according to each participant’s annotations with the following method: if a volunteer divided the objects into n levels in stiffness and friction dimensions, each level was assigned values of $0, \frac{1}{n-1}, \frac{2}{n-1}, \dots, 1$. This mapped all ratings to the 0-1 range and ensured comparability across different numbers of levels. Fig. 4D shows the average heatmaps of three tactile semantic dimensions corresponding to the ground truth maps. Quantitatively, the Intersection over Union (IoU) between the sketched shapes and the ground truth was consistently high (Fig. 4E, left plot). The overall mean IoU across all objects and participants was 0.45 ± 0.15 , with the mean IoU for individual objects ranging from 0.40 to 0.54. This demonstrates that the rendered multidimensional tactile information is clear, discriminable, and allows for accurate spatial perception.

Task 2: Object Identification and Placement This task assessed participants’ ability to identify and spatially arrange objects under two distinct conditions. First, participants performed an unrestricted task in which they had to both select objects from eight alternatives and place them on a canvas as precisely as possible. Second, they performed a constrained task where they were informed of the correct object sets and only had to place them. Overall, participants demonstrated high accuracy, with performance significantly improving when offered the right object sets. In the unrestricted condition, the mean placement accuracy was $66.7 \pm 32.5\%$ for Scene 1 and $53.4 \pm 27.1\%$ for Scene 2. Accuracy rose sharply in the constrained condition to $93.9 \pm 19.6\%$ for Scene 1 and $87.5 \pm 24.1\%$ for Scene 2. The results are visualized in the average placement maps (Fig. 4F), and the quantitative results are presented in Fig. 4E (right plot). Notably, the median accuracy of 1.0 in the constrained tasks indicates that most participants achieved perfect placement. These results confirm that users can precisely perceive both object identities and their spatial arrangements from

the rendered haptic feedback alone.

Tele-Touch Experiment for Remote Object Perception

Our haptic system renders high-fidelity, multidimensional tactile information. Its ability to couple the rendering of complex geometries with continuously variable stiffness and friction makes it a powerful platform for a wide range of downstream applications, from industrial quality control and remote robotics to immersive training simulations. To demonstrate its potential in a challenging domain, we developed a novel Tele-Touch system for remote medical palpation. The system’s architecture (Fig. 5A) consists of a remote site and a local site connected by a bidirectional flow of data. At the remote site, a robotic arm equipped with a tactile sensor traverses the surface of a tumor phantom, whose internal structure is shown in Fig. 5B, capturing shape information directly and inferring stiffness from force-indentation data. At the local site, the user teleoperates the arm using our sliding platform, receiving the rendered haptic feedback. A graphical user interface (Fig. 5C) and a live video feed (Fig. 5D) provide real-time positional guidance for exploration.

To evaluate the system’s effectiveness, we designed two opaque, flesh-like silicone tumor phantoms to simulate clinical scenarios (Fig. 5B) for two specific tasks. For the “Tumor Localization” task, the phantom contained tumors of identical size and material. For the “Property Discrimination” task, the phantom contained tumors of varying size to simulate growth, and of varying hardness (soft silicone vs. hard polylactic acid, PLA) to simulate changes in severity or malignancy. We then conducted these two experiments using the above setup. A detailed implementation of the phantoms and experimental procedures is described in the Materials and Methods section, Tele-Touch Pipeline part.

Task 1: Tumor Localization In this task, participants were asked to determine the number and position of tumors, which were embedded at random locations within the phantom tissue. The results in Fig. 5E and Fig. 5F show that they successfully identified all tumors and located the tumors with high accuracy. In Fig. 5E, the participant-identified centers show tight clustering around the ground truth locations. Fig. 5F shows that the distance error between the identified and ground truth centers was consistently low. The mean localization error was 0.34 ± 0.15 cm for the first tumor and 0.41 ± 0.17 cm for the second, with an overall mean error of 0.37 ± 0.16 cm. This high accuracy

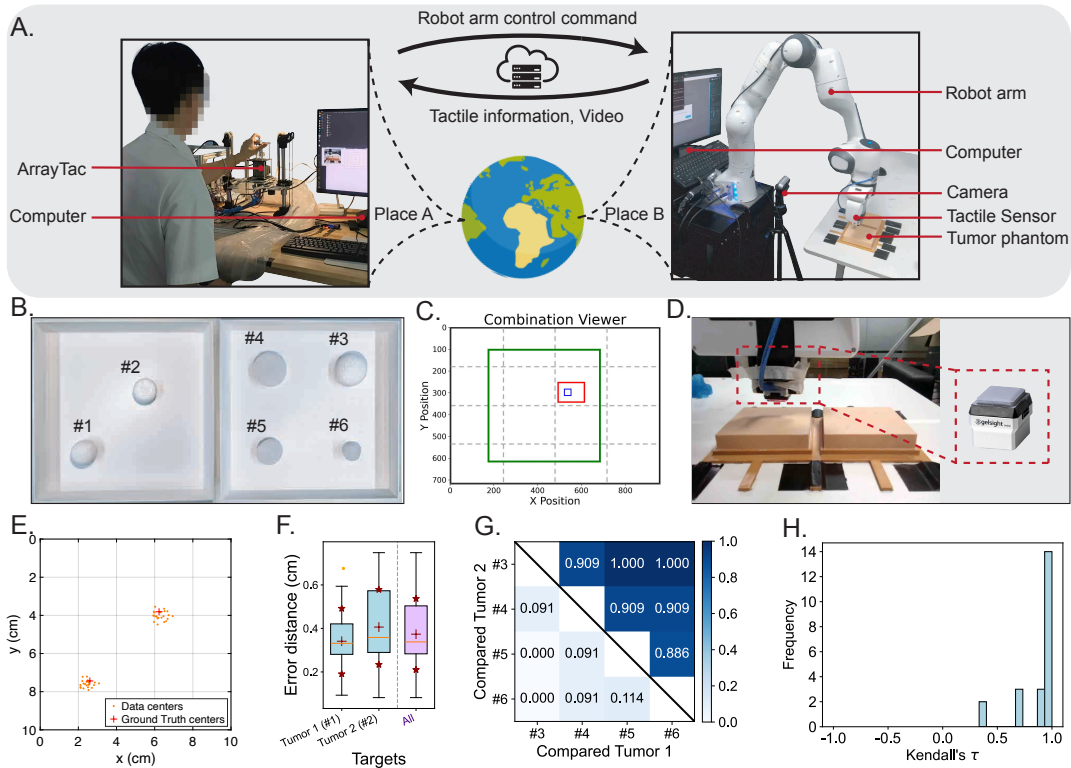


Figure 5: Experimental Setup and Results for the Tele-Palpation Task. (A) The architecture of the Tele-Touch system. Operators can use the ArrayTac interface locally to manipulate robotic arms located anywhere in the world and perceive remote tactile information. Data streams are transmitted through a cloud server to enable real-time interaction. (B) Internal design of the two tumor phantom tissue models. The left phantom was used for the “Tumor Localization” task, while the right phantom was used for the “Property Discrimination” task. (C) The graphical user interface (GUI) for system control. (D) Screenshot of the real-time video viewed by participants during the experiment, showing a GelSight tactile sensor mounted on the robotic arm’s end effector. (E) Visualized results for the tumor localization task ($n = 22$). (F) Quantitative analysis of localization error ($n = 22$). The box plot shows the distance between participant-identified centers and the ground truth for two targets and the aggregated data. (G) Pairwise preference heatmap for the tumor severity ranking task ($n = 22$). Each cell value represents the percentage of participants who perceived “Compared Tumor 2” (Y-axis) as more severe/harder than “Compared Tumor 1” (X-axis). (H) Distribution of Kendall’s tau (τ) coefficients for the severity ranking data ($n = 22$).

demonstrates that the proposed Tele-Touch framework exhibits outstanding performance in remote tumor palpation and localization.

Task 2: Tumor Property Discrimination For the property discrimination task, participants were asked to judge the severity of four tumors. They needed to rank them according to the stiffness and size they perceived through the rendered haptic feedback. The results demonstrate a high degree of accuracy and consensus. The pairwise preference heatmap in Fig. 5G exhibits a strong positive rate in the upper triangular, indicating that participants were able to rank the tumors' severity reliably. To further quantify this, we calculated Kendall's Tau (τ) coefficient for each participant's ranking in Fig. 5H. Kendall's Tau is a statistic that measures the ordinal association between the participant's ranking and the ground truth, where a value of $\tau = 1$ indicates a perfect match. The distribution of these coefficients shows a strong concentration of values near 1.0, with a mean τ of 0.88 ± 0.21 . This strong, correct correlation confirms that users could reliably discern the property of the tumors, indicating that our proposed Tele-Touch framework can precisely transmit fine tactile details from remote environments back to the user, enabling accurate remote assessment of tumors.

In summary, the results from both the localization and discrimination tasks demonstrate that our proposed Tele-Touch framework can accurately transmit fine tactile details from remote environments to the user, enabling precise tumor localization and reliable diagnosis of tumor properties. These validate its potential for meaningful Tele-Touch applications such as remote medical examination.

Cross-city Remote Breast Tumor Palpation over 1000 km

The realization of remote palpation carries profound clinical and social implications, potentially enabling patients in remote areas to access expert diagnostic support from specialists at major medical centers. Given that palpation is a critical primary screening method for breast tumors, we selected it as our experimental scenario. Under the Tele-Touch framework, 11 naive volunteers in City A (Fig. 6A) operated the ArrayTac device to remotely control a robotic palpation station deployed over 1,000 km away in City B (Fig. 6B). At this remote site, the system interacted with a medical-grade breast tumor training phantom (Fig. 6C), which contained two concealed tumors in the right breast: one malignant and one benign. Despite a straight-line distance exceeding 1,000 km

between the two cities, the system maintained a maximum end-to-end latency of under 0.1 s for both control and sensory signals.

None of the volunteers possessed prior medical expertise. Prior to the task, they were provided with only a basic diagnostic heuristic stating that malignant breast tumors typically exhibit unclear boundaries and uneven surfaces, whereas benign tumors generally have distinct boundaries and smooth surfaces. Relying on the haptic feedback rendered by ArrayTac, supplemented only by a live camera feed (Fig. 6D) and a GUI (Fig. 6E) for end-effector spatial positioning, participants were asked to determine the number, location, and nature of the hidden tumors, and recording their findings on paper.

The experimental results were striking: all 11 participants successfully identified the number and the nature of tumors, achieving a 100% diagnostic accuracy rate. The spatial localization results from the volunteers are illustrated in Fig. 6F and Fig. 6G. Quantitative analysis revealed a mean localization error of 0.77 ± 0.45 cm for the benign tumor, compared to 0.84 ± 0.49 cm for the malignant mass. It can be observed that the volunteers' localization precision for the malignant tumor was slightly higher error than that for the benign tumor, which may be related to the unclear boundaries of the malignant tumor.

User Experience and System Performance Evaluation

To quantitatively evaluate the system's usability and the overall user experience, we conducted a study where 22 participants completed two standard questionnaires—the System Usability Scale (SUS) and the USE questionnaire (49)—after performing the main experimental tasks. The SUS provided a standardized, single-score benchmark of overall usability, while the USE questionnaire was employed to gather detailed, multidimensional feedback on subjective aspects. The original USE questionnaire was adapted by removing inapplicable items and adding a new dimension: Performance. The detailed questionnaires can be found in Supplementary Materials (User Questionnaire Survey). The feedback from both questionnaires was overwhelmingly positive, indicating that the system is not only highly usable but also provides an enjoyable and intuitive experience.

For the System Usability Scale (SUS), scores were calculated using the standard method (50): for odd-numbered (positive) items, the score contribution is the scale position minus 1; for even-

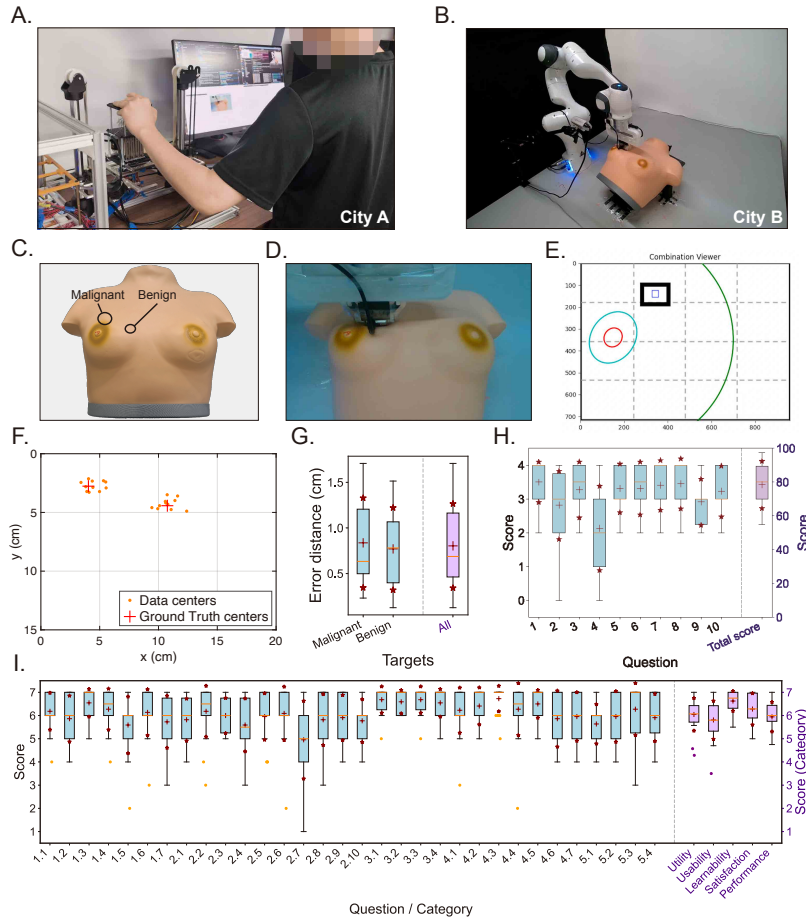


Figure 6: Cross-city remote breast tumor palpation experiment and quantitative user experience evaluation. (A) The local teleoperation setup in City A, where a naive volunteer operates ArrayTac. (B) The remote site in City B (>1000 km away), where a robot arm performs real-time palpation with sub-0.1s latency. (C) The medical-grade breast phantom containing an embedded malignant and a benign tumor. (D) The Screenshot of the real-time video viewed by participants during the experiment. (E) The GUI provides continuous positional information for the end effector. (F) Visualized results for the tumor localization task ($n = 11$). (G) Quantitative analysis of localization error ($n = 11$). (H) Distribution of the final calculated SUS scores from all participants, presented as a box plot. The scores are converted from their raw 5-point scale responses to a final 100-point scale using the standard calculation method for standardized benchmarking. For a single question, the scores are converted to 0-4 for easy comparison ($n = 22$). (I) Distribution of scores for each question in the USE questionnaire, presented as box plots ($n = 22$).

numbered (negative) items, it is 5 minus the scale position. The sum of these converted scores was then multiplied by 2.5 to yield a final score on a 0-100 scale (Fig. 6H). Meanwhile, all items in the USE questionnaire were rated on a standard 7-point Likert scale.

The System Usability Scale (SUS) benchmark yielded a score of 78.41 ± 13.92 (Fig. 6H). According to established benchmarks, this score places the system in the top quartile of products tested, corresponding to an “A-” grade and classifying its usability as “excellent” (51). The results show consistently strong ratings, with 9 of the 10 questions achieving a median score of 3 or higher (on a 0-4 scale). This high score was driven by perfect median ratings on key items, including a strong desire for frequent use (Q1), a strong agreement that the system is easy to learn (Q7), and a strong disagreement that it is cumbersome to use (Q8). The one area for improvement was user independence, with a neutral median score for needing technical support (Q4), reinforcing that initial guidance is beneficial.

Consistent with the SUS benchmark findings, the USE questionnaire revealed a highly positive, comprehensive subjective experience. The consistency of this feedback is underscored by the fact that 30 out of 32 individual questionnaire items achieved a median score of 6 or higher. Overall, the system received strong average scores across all five evaluated dimensions: Usefulness (6.05 ± 0.70), Ease of Use (5.81 ± 0.82), Learnability (6.63 ± 0.43), Satisfaction (6.28 ± 0.68), and our custom Performance metric (5.94 ± 0.64) (Fig. 6I). This reception was exceptionally strong in learnability, where all items received a perfect median score of 7. Similarly, key satisfaction metrics (“I would recommend it to a friend”) and core technical capabilities like friction rendering (“I think the device distinguishes friction well”) also achieved perfect median scores, highlighting a genuinely enjoyable and effective user experience. The only notable exception was the item “I can use it without written instructions” (median=5), suggesting a brief introduction helps users achieve full confidence.

Discussion

In this work, we presented ArrayTac, a high-performance piezoelectric tactile display that pioneers the simultaneous rendering of an object’s shape, stiffness, and friction on a unified platform. To achieve this, the system integrates a novel three-stage micro-lever mechanism with high-frequency

closed-loop control, which delivers a 5 mm displacement and a 123.39 Hz bandwidth. Consequently, ArrayTac enables true zero-shot identification: naive users can intuitively recognize complex 3D shapes and physical properties without prior training, effectively bridging the cognitive gap inherent in traditional haptic mappings.

Beyond hardware innovation, we integrated ArrayTac into two end-to-end application pipelines. Tac-Anything leverages foundation multimodal models to automatically extract and render tactile semantics directly from 2D images. Furthermore, our Tele-Touch framework validated the system’s clinical viability through a >1,000 km cross-city palpation task. Maintaining sub-0.1s latency, naive operators achieved 100% diagnostic accuracy in distinguishing breast tumor phantoms. These impressive results strongly validate the system’s immense potential for meaningful Tele-Touch applications, such as remote medical examinations.

We acknowledge several limitations in the current study that open avenues for future research. While we successfully utilized a sliding platform to achieve haptic super-resolution and an expanded workspace, resulting in excellent experimental outcomes, further increasing the scale of the actuator array (e.g., 8×8 or 16×16) could further enhance the system’s display capabilities. Additionally, our friction rendering is a simplification that relies solely on vibrotactile cues and does not reproduce the tangential force inherent in real-world friction. Finally, incorporating more sophisticated physical models, such as viscoelastic models, will better capture the properties of complex soft materials. Overall, ArrayTac provides a foundation for the next generation of immersive human-computer interaction.

Materials and Methods

Tactile Display System Design and Fabrication

The tactile display system was engineered as an integrated haptic device. The hardware architecture consists of two main components: the mechanical structure and the driving circuitry.

Mechanical Structure As shown in Fig. 7A, the core of the ArrayTac system is a compact 4×4 actuator array, consisting of 16 independently addressable actuator units. Each unit ($12.4 \times 8.4 \times 76$ mm) integrates a piezoelectric ceramic element, a three-stage micro-lever amplification

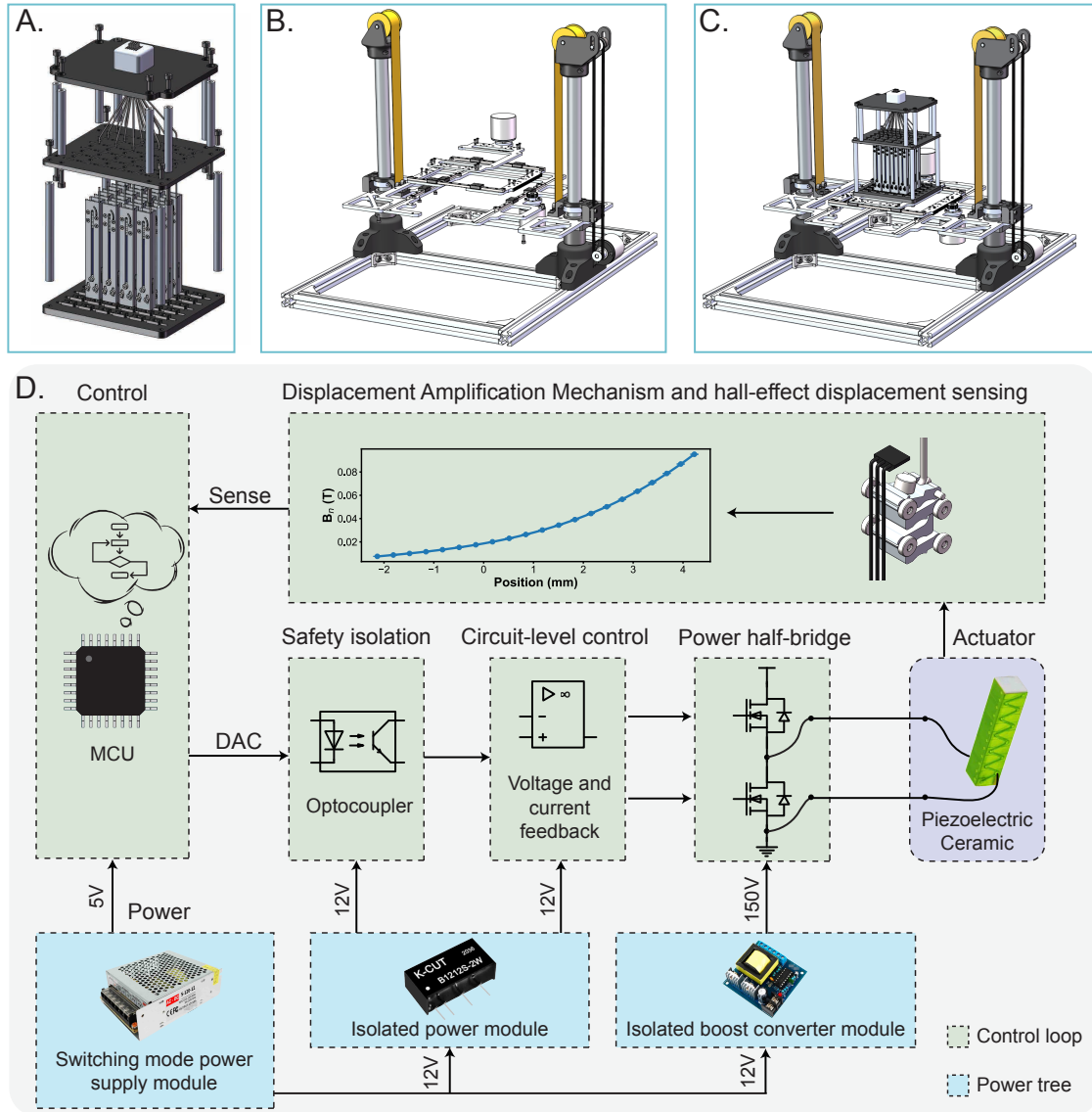


Figure 7: System Design and Schematics. (A) Exploded view of the actuator array. (B) Exploded view of the XYZ sliding stage. (C) Assembled view of the interactive platform. (D) The circuit schematic for an individual ArrayTac unit, comprising the control circuit and the power tree.

mechanism, a Hall effect sensor, and an end-effector steel wire. The piezoelectric ceramic (DCS3-050536) generates a displacement of up to 40 μm , which is amplified 125-fold by the lever system to produce a 5 mm stroke transmitted through a bent steel wire. An axially magnetized NdFeB magnet is mounted on the final lever stage and paired with a Hall sensor (A1324) for closed-loop position feedback. The housing and levers are made of AISI 1045 steel, which provides magnetic shielding and structural stability.

As illustrated in Fig. 1D, the actuator's compact form factor allows dense array integration, while the internal lever system, shown in Fig. 1E, is fabricated via precision wire electrical discharge machining (EDM) to ensure consistent amplification ratios. A fine-threaded adjustment base beneath the piezoelectric element allows accurate height calibration during assembly, compensating for machining and installation tolerances.

The entire actuator array is mounted on a three-degree-of-freedom zero-gravity sliding platform, as shown in Fig. 7B and Fig. 7C. This mechanism expands the tactile workspace to $60 \times 60 \times 185$ mm in the X-Y-Z directions. Orthogonal linear guide rails and low-friction bearings ensure smooth motion, while constant-force springs provide vertical counterbalance, creating a near-weightless interaction experience. The platform's movement is measured through rack-and-pinion and belt-driven rotary encoders, enabling precise, real-time 3D coordinate tracking for synchronized tactile rendering.

Drive Circuits Design The circuit schematic for an individual ArrayTac unit, illustrated in Fig. 7D, comprises a closed-loop displacement control system and a multi-level power tree. The core of the entire control loop is a microcontroller unit (MCU), whose control signals are output by two DAC channels and serve as the reference input for circuit-level control after passing through an optocoupler for high-low voltage isolation. The circuit-level controller, composed of operational amplifiers, respectively controls the upper and lower arms of the power half-bridge. It establishes voltage negative feedback for the charging voltage and current negative feedback for the discharging current of the piezoelectric ceramic, thereby achieving high-speed control of the ceramic's voltage. The output of the piezoelectric ceramic, after being amplified by a micro-lever, drives the movement of a permanent magnet, which in turn causes a change in the Hall sensor's reading. After calibration, the displacement of the lever's end can be obtained. This is then used as the feedback input to the

MCU to complete the construction of the control loop. The power for the entire system is supplied by a switching power supply. Its 5V output is used to supply low-voltage systems such as the MCU. Its 12V output, after being transformed by an isolated power module, is used to provide an isolated power source for the optocoupler and operational amplifiers, ensuring safety and driving capability. This 12V is also stepped up to 150V by an isolated boost converter module to serve as the input for the power half-bridge, used to drive the piezoelectric ceramic for full-range actuation.

More detailed information on the fabrication and assembly of the mechanical and electronic components is in the Supplementary Materials (Tactile Display System Design and Fabrication).

High-Fidelity Shape Rendering System: Design and Validation

Conventional open-loop tactile displays are susceptible to force disturbances from user interaction, which limits their fidelity. To overcome this limitation, we implemented a closed-loop position control system for each of the 16 actuator units. At the core of each unit, a small NdFeB magnet was fixed on the final lever stage, positioned beneath a linear Hall effect sensor. The sensor measured the change of magnetic flux density, which correlated to the end-effector's vertical displacement, and this analog signal was processed by an onboard microcontroller as the position feedback. Using this real-time feedback, the microcontroller controlled the voltage applied to the piezoelectric element through a Proportional-Integral-Derivative (PID) controller, thereby achieving closed-loop position control. We conducted rigorous experiments to illustrate the accuracy of the sensor feedback model and quantify the dynamic performance benefits of the closed-loop architecture.

Validation of the Sensor-to-Displacement Model A robust model mapping the Hall sensor's voltage output to physical displacement was established and validated through both simulation and physical experiments. First, the sensor's nonlinear response was modeled in Ansys Maxwell EDT software, where a simulation of the actuator components (Fig. 2A) revealed that a cubic polynomial provides an exceptionally accurate fit to the data ($R^2 = 0.999$) and is robust to potential assembly variations (Fig. 2B). To confirm these simulation results on the physical hardware, the model was then validated on all 16 fabricated actuators. The results were highly consistent with the simulation; applying the same cubic polynomial fit yielded a precise model for every unit, each achieving a coefficient of determination greater than 0.997 (Fig. 2C). This strong agreement confirmed that our

model provides an accurate and reliable method for tracking the end-effector’s position.

Closed-Loop Control Dramatically Improves Dynamic Performance To generate realistic and responsive haptic feedback, the display must operate with high speed and stability. We evaluated the actuator performance using step and frequency response tests, with fingertip loading simulated by soft silicone. The results confirmed that closed-loop control is critical for achieving high performance. As shown in Fig. 2D, the step response under overdamped closed-loop control exhibited zero steady-state error, with rise and fall times of 0.013 s and 0.016 s, respectively, ensuring that the device can render sharp features without overshoot. More critically, frequency response analysis revealed a dramatic enhancement in control bandwidth. We use the frequency sweep method to plot the system’s Bode plot. According to engineering convention, the system bandwidth is defined as the minimum of the -3 dB amplitude cutoff frequency and the -90° phase cutoff frequency. Under the open-loop control, the system (Fig. 2E) had a limited bandwidth of only 15.29 Hz, while using closed-loop control (Fig. 2F) could expand this by more than eightfold to 123.39 Hz. This substantial increase in bandwidth is what enables the system to effectively compensate for mechanical attenuation and render the complex, high-frequency cues essential for realistic, real-time haptic sensations.

Nonlinear Stiffness Rendering Method

Our method for rendering nonlinear stiffness utilizes a two-stage hybrid control strategy, the architecture of which is detailed in the block diagram in Fig. 8A. This architecture combines a primary PID closed-loop controller, which provides high-fidelity position tracking, with a secondary feedforward penalty control. A saturation limit on the PID controller’s output acts as a crucial switch: when the force required to maintain position exceeds this limit, the feedforward penalty is engaged. This two-stage design was specifically developed to replicate the complex force-displacement profiles of real-world soft materials. As an example, the stress-strain curve for High Resilience (HR) foam, shown in Fig. 8B, exhibits a distinct biphasic response (52). The two stages of our controller map directly onto this profile: the PID-dominant stage reproduces the initial high-stiffness phase (Region A), while the feedforward penalty stage reproduces the subsequent, softer yielding phase (Region B). A single normalized parameter, k , is used to modulate the rendered stiffness across

this entire profile.

The control law employs a two-stage approach to replicate this biphasic behavior. First, to quantitatively emulate the high surface stiffness of region A, the system calculates a defined voltage threshold, U_{limit} :

$$U_{\text{limit}} = \frac{k + 4}{5} \cdot (U_{\text{max}} - U_{\text{base}}) + U_{\text{base}}, \quad (1)$$

where k is the normalized stiffness parameter. Below this output voltage, the system employs PID closed-loop control to maintain the lever tip precisely at the target position without deviation. Once the required control effort exceeds U_{limit} , the PID output reaches saturation and the feedforward control takes over, where represents the material's yield point. After this point, a nonlinear penalty term is introduced to emulate the yielding behavior of region B. The final output voltage, U_{output} , is then calculated as:

$$U_{\text{output}} = (U_{\text{limit}} - U_{\text{base}}) \cdot \left(1 - (1 - k) \cdot \frac{\epsilon}{x_{\text{piezo_limit}}} \right)^n + U_{\text{base}}, \quad (2)$$

where ϵ denotes the error of the piezoelectric ceramic displacement, $x_{\text{piezo_limit}}$ is the maximum piezoelectric ceramic displacement achieved under the voltage U_{limit} when the end-effector is unloaded, and it can be readily computed on the microcontroller using U_{limit} , U_{base} , and the piezoelectric voltage-displacement coefficient β . The exponent n governs the nonlinearity of the penalty. A detailed derivation of the underlying physical model is provided in the Supplementary Materials (Theoretical Modeling and Control for Stiffness Rendering).

Validation of the Nonlinear Control Law To select the optimal penalty exponent n , we evaluated first, second, and third-order penalties ($n = 1, 2, 3$) through simulation and physical testing. Although MATLAB simulations indicated that larger nonlinear penalties ($n > 1$) produced more realistic biphasic curves (Fig. 8C), the third-order penalty ($n = 3$) proved unstable on the physical hardware. Consequently, a quadratic penalty ($n = 2$) was adopted as the optimal compromise between realism and stability. A separate mathematical derivation also supported this choice in Supplementary Materials (Theoretical Justification for the Nonlinear Control Law), further indicating that the effective range for the stiffness parameter is $k > 0.5$ when $n = 2$. The measured performance of the system using this validated controller is shown in Fig. 8D. The resulting force-displacement curves confirm that, for $k > 0.5$, the controller successfully reproduces the characteristic bipha-

sic profile of HR foam, exhibiting a clear correspondence with the high-stiffness (Region A) and yielding (Region B) phases shown in Fig. 8B. Furthermore, the normalized stiffness parameter k provides control over the stiffness, simultaneously modulating both the initial resistance (the y-axis intercept in Region A) and the yielding behavior (the slope in Region B). This result demonstrates that our control law enables each actuator to replicate the subtle tactile characteristics of complex nonlinear materials while offering tunable stiffness modulation.

Calibration to Standard Stiffness Metrics To ground the abstract control parameter k in a physical measurement, we developed a calibration procedure that follows the principle of Shore hardness—an industrial standard that quantifies stiffness by measuring a material’s resistance to indentation. We specifically used the Shore 00 scale, which is designed for the ultra-soft range of materials that includes the homogeneous soft objects and fabricated silicone blocks in our dataset. Based on this principle, we designed an equivalent reference device with an identical end-contact surface to that of the tactile display (Fig. 8E). By applying the same pressure and aligning the resulting deformation, we calibrated the correspondence between the parameter k and the shore 00 value. We first measured the deformation of each object under three different constant normal forces ($F_n = 1, 1.5, 2$ N), with the results shown in Fig. 8F. We then adjusted the parameter k on our haptic display until its end-effector produced the same deformation under the same applied force. This procedure yielded a robust, near-linear mapping between the calibrated k values and the measured Shore 00 stiffness (Fig. 8G). A linear regression model was fitted to these data, establishing a direct and reliable link between our device’s rendered stiffness and a standard industrial material property.

Tac-Anything Framework

To enable users to perceive tactile properties from a single 2D image, we developed the Tac-Anything framework. Although previous studies have explored image-to-touch conversion, these approaches were limited to transforming scenes into predefined symbolic patterns. Such representations often fail to align with natural haptic semantics and sensory intuition, and they typically lack real-time rendering capability (53). However, Tac-Anything extracts comprehensive tactile information from only a photo, including shape, stiffness, and friction. It then renders the information in real-time on ArrayTac. The framework’s architecture is illustrated in Fig. 4A. The workflow begins with a single

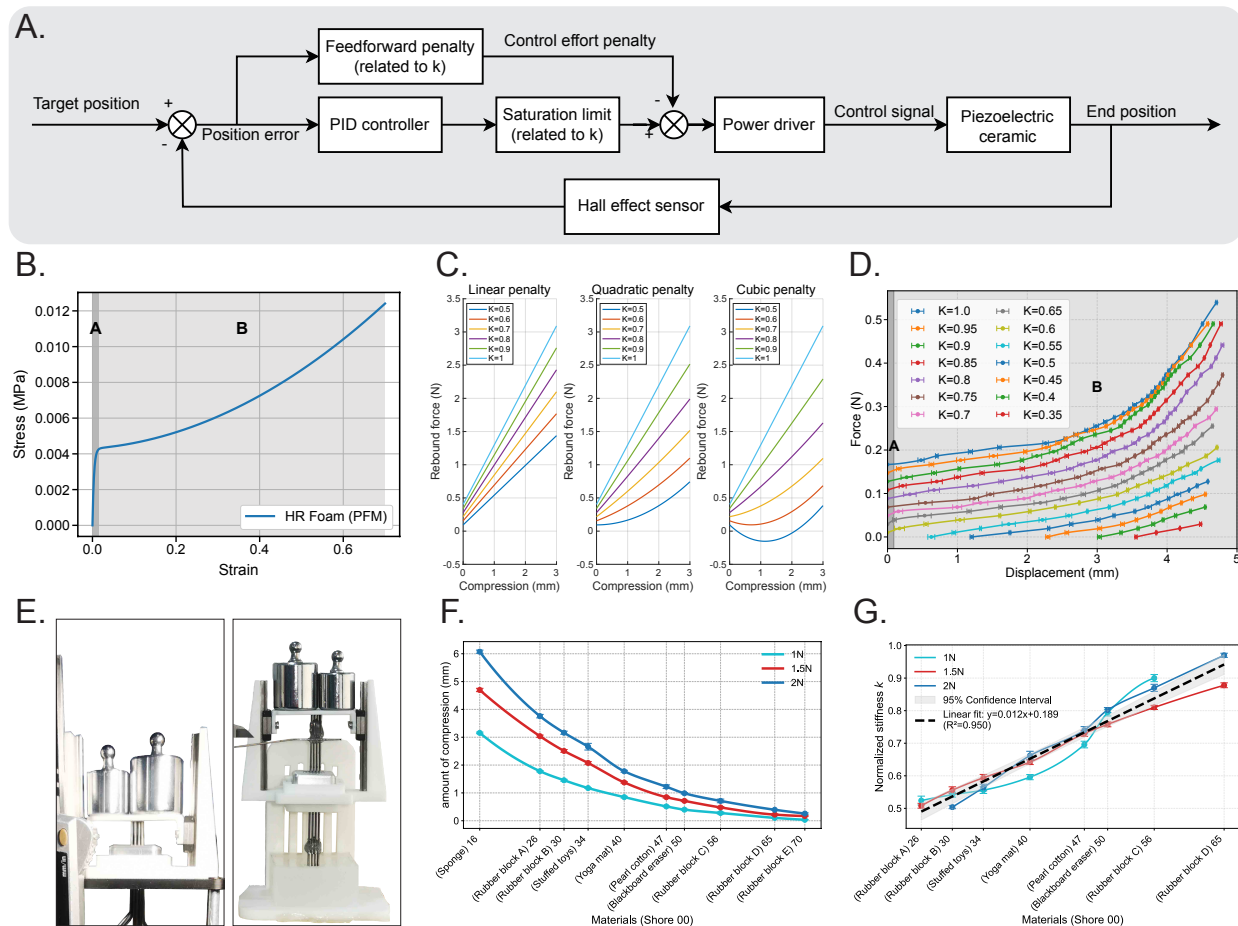


Figure 8: Unit stiffness control method and performance. (A) Block diagram of the stiffness control algorithm. (B) Strain-stress curve of HR foam derived from a mathematical model. (C) MATLAB-simulated displacement-force curves of the display unit under different penalty orders. (D) Experimentally measured displacement-force curves of the display unit under different normalized stiffness parameters k ($n = 8$). (E) Experimental setup for aligning normalized stiffness with measured Shore 00 stiffness. (F) Compressive deformation and corresponding Shore 00 stiffness of common household objects under different applied pressures ($n = 5$). (G) Relationship between normalized stiffness k and Shore 00 stiffness ($n = 5$).

RGB image as input, which is processed simultaneously through two parallel deep learning pathways. In the first pathway, the system reconstructs the surface topography. The image is processed by the Depth-Anything-V2 model (54) to perform monocular depth estimation. This step generates a dense depth map (the “Depth layer”) that represents the scene’s 3D shape. Concurrently, the second pathway determines material properties. The image is sent to the Segment-Anything model (55), which identifies and isolates the main objects. This process generates distinct “segments” and their corresponding masks. Each isolated segment is then analyzed by a Vision Language Model (VLM). The VLM leverages its world knowledge to infer quantitative tactile properties, such as a “Shore 00 stiffness of 16” and a “relative friction of 0.3”. This inferred data is aligned with the object masks to create the “Stiffness” and “Friction” layers. Finally, the three generated layers—Depth, Stiffness, and Friction—are spatially aligned and stacked. This creates a unified “tactile semantic high-dimensional array.” The array is then sampled in real-time based on the user’s interaction and streams the tactile information to ArrayTac, allowing users to perceive the tactile properties from the input image.

Tele-Touch Pipeline

We construct a Tele-Touch system to validate ArrayTac’s performance in a remote touch scenario. The architecture of this system is illustrated in Fig. 5A. The system is divided into two sites: a local site (Site A) and a remote site (Site B), with communication established via a cloud-based TCP server. Site A consisted of our haptic display and the user, while Site B comprised a Franka robotic arm equipped with a GelSight visuotactile sensor and the target materials for palpation.

During operation, the user at Site A manipulates the tactile display, moving it in XYZ space. This movement is translated into commands that teleoperate the robotic arm at Site B, enabling it to explore and press the target materials in three dimensions. Simultaneously, the GelSight sensor at the remote site captures high-resolution tactile information upon contact. This data is processed and transmitted back to the display at Site A for real-time haptic rendering. The feedback includes shape information, which is read directly from the GelSight sensor, and stiffness information, which is calculated as the ratio of the applied normal force to the measured compression depth. As friction is considered less critical for this palpation task, its value was preset to 0.

References and Notes

1. D. Wang, K. Ohnishi, W. Xu, Multimodal haptic display for virtual reality: A survey. *IEEE Transactions on Industrial Electronics* **67** (1), 610–623 (2019).
2. H. Kajimoto, S. Saga, M. Konyo, *Pervasive Haptics* (Springer) (2016).
3. V. G. Chouvardas, A. N. Miliou, M. K. Hatalis, *et al.*, Tactile displays: a short overview and recent developments. *Proceedings of the ICTA* pp. 246–251 (2005).
4. K. A. Kaczmarek, J. G. Webster, P. Bach-y Rita, W. J. Tompkins, Electrotactile and vibrotactile displays for sensory substitution systems. *IEEE transactions on biomedical engineering* **38** (1), 1–16 (2002).
5. S. Biswas, Y. Visell, Haptic perception, mechanics, and material technologies for virtual reality. *Advanced Functional Materials* **31** (39), 2008186 (2021).
6. N. A. Mansour, A. M. F. El-Bab, M. Abdellatif, Design of a novel multi-modal tactile display device for biomedical applications, in *2012 4th IEEE RAS & EMBS International Conference on Biomedical Robotics and Biomechatronics (BioRob)* (IEEE) (2012), pp. 183–188.
7. J. Colan, A. Davila, Y. Hasegawa, Tactile Feedback in Robot-Assisted Minimally Invasive Surgery: A Systematic Review. *The International Journal of Medical Robotics and Computer Assisted Surgery* **20** (6), e70019 (2024).
8. W. Dangxiao, *et al.*, Haptic display for virtual reality: progress and challenges. *Virtual Reality & Intelligent Hardware* **1** (2), 136–162 (2019).
9. S. Okamoto, H. Nagano, Y. Yamada, Psychophysical Dimensions of Tactile Perception of Textures. *IEEE Transactions on Haptics* **6** (1), 81–93 (2013), doi:10.1109/TOH.2012.32.
10. Z. Xue, *et al.*, Arraybot: Reinforcement learning for generalizable distributed manipulation through touch, in *2024 IEEE International Conference on Robotics and Automation (ICRA)* (IEEE) (2024), pp. 16744–16751.

11. A. F. Siu, E. J. Gonzalez, S. Yuan, J. B. Ginsberg, S. Follmer, Shapeshift: 2D spatial manipulation and self-actuation of tabletop shape displays for tangible and haptic interaction, in *Proceedings of the 2018 CHI Conference on Human Factors in Computing Systems* (2018), pp. 1–13.
12. D. Trinitatova, D. Tsetserukou, FiDTouch: A 3D Wearable Haptic Display for the Finger Pad. *arXiv preprint arXiv:2507.07661* (2025).
13. P. Kammermeier, M. Buss, G. Schmidt, Dynamic display of distributed tactile shape information by a prototypical actuator array, in *Proceedings. 2000 IEEE/RSJ International Conference on Intelligent Robots and Systems (IROS 2000)(Cat. No. 00CH37113)* (IEEE), vol. 2 (2000), pp. 1119–1124.
14. Y. Herbst, A. Wolf, L. Zelnik-Manor, HUGO, a high-resolution tactile emulator for complex surfaces, in *Proceedings of the 2023 CHI Conference on Human Factors in Computing Systems* (2023), pp. 1–15.
15. M. M. H. Saikot, K. R. I. Sanim, Refreshable braille display with adjustable cell size for learners with different tactile sensitivity. *IEEE Transactions on Haptics* **15** (3), 582–591 (2022).
16. D. Chen, *et al.*, Design and Evaluation of an Electromagnetic Bounce-Type Refreshable Braille Display. *IEEE Transactions on Neural Systems and Rehabilitation Engineering* (2025).
17. T. Iwamoto, H. Shinoda, Ultrasound tactile display for stress field reproduction-examination of non-vibratory tactile apparent movement, in *First Joint Eurohaptics Conference and Symposium on Haptic Interfaces for Virtual Environment and Teleoperator Systems. World Haptics Conference* (IEEE) (2005), pp. 220–228.
18. T. Hoshi, M. Takahashi, T. Iwamoto, H. Shinoda, Noncontact tactile display based on radiation pressure of airborne ultrasound. *IEEE transactions on haptics* **3** (3), 155–165 (2010).
19. H. Kajimoto, Electro-tactile display: principle and hardware, in *Pervasive Haptics: Science, Design, and Application* (Springer), pp. 79–96 (2016).

20. Q. Xiong, *et al.*, Virtual tactile feedback technology based on microcurrent stimulation: current status, challenges and future prospects. *Frontiers in Neuroscience* **19**, 1519758 (2025).
21. P.-H. Chu, *et al.*, A Compact Electro-tactile System for Braille Display, in *2024 46th Annual International Conference of the IEEE Engineering in Medicine and Biology Society (EMBC) (IEEE)* (2024), pp. 1–4.
22. E. AliAbbasi, *et al.*, Effect of finger moisture on tactile perception of electroadhesion. *IEEE Transactions on Haptics* (2024).
23. S. Kim, P. Kim, C.-Y. Park, S.-B. Choi, A new tactile device using magneto-rheological sponge cells for medical applications: Experimental investigation. *Sensors and Actuators A: Physical* **239**, 61–69 (2016).
24. I. Hwang, *et al.*, Height-renderable morphable tactile display enabled by programmable modulation of local stiffness in photothermally active polymer. *Nature Communications* **15** (1), 2554 (2024).
25. P. S. Wellman, W. J. Peine, G. Favalora, R. D. Howe, Mechanical design and control of a high-bandwidth shape memory alloy tactile display, in *Experimental Robotics V: The Fifth International Symposium Barcelona, Catalonia, June 15–18, 1997* (Springer) (2007), pp. 56–66.
26. S.-Y. Jang, *et al.*, Dynamically reconfigurable shape-morphing and tactile display via hydraulically coupled mergeable and splittable PVC gel actuator. *Science Advances* **10** (39), eadq2024 (2024).
27. C. Tian, *et al.*, Dynamic braille display based on surface-structured PVC gel. *Smart Materials and Structures* **33** (3), 035018 (2024).
28. Y. Ujitoko, T. Taniguchi, S. Sakurai, K. Hirota, Development of finger-mounted high-density pin-array haptic display. *IEEE Access* **8**, 145107–145114 (2020).
29. J. Jeong, M. Kang, Y. Song, S. Pyo, Interactive Haptic System with Multimodal Tactile Sensing and Hydraulic Feedback for Realistic Human–Machine Interaction. *Advanced Intelligent Systems* **7** (5), 2400578 (2025).

30. B. Shan, *et al.*, A Multi-Layer Stacked Microfluidic Tactile Display With High Spatial Resolution. *IEEE Transactions on Haptics* **17** (4), 546–556 (2024).
31. T. Ninomiya, K. Osawa, Y. Okayama, Y. Matsumoto, N. Miki, MEMS tactile display with hydraulic displacement amplification mechanism, in *2009 IEEE 22nd International Conference on Micro Electro Mechanical Systems (IEEE)* (2009), pp. 467–470.
32. L. Liu, Y.-G. Bai, D.-L. Zhang, Z.-G. Wu, Ultra-precision measurement and control of angle motion in piezo-based platforms using strain gauge sensors and a robust composite controller. *Sensors* **13** (7), 9070–9084 (2013).
33. K.-U. Kyung, M. Ahn, D.-S. Kwon, M. A. Srinivasan, A compact broadband tactile display and its effectiveness in the display of tactile form, in *First Joint Eurohaptics Conference and Symposium on Haptic Interfaces for Virtual Environment and Teleoperator Systems. World Haptics Conference (IEEE)* (2005), pp. 600–601.
34. J. G. Linvill, J. C. Bliss, A direct translation reading aid for the blind. *Proceedings of the IEEE* **54** (1), 40–51 (2005).
35. M. Kobayashi, T. Watanabe, A tactile display system equipped with a pointing device—MIMIZU, in *International Conference on Computers for Handicapped Persons* (Springer) (2002), pp. 527–534.
36. G.-H. Yang, K.-U. Kyung, M. A. Srinivasan, D.-S. Kwon, Quantitative tactile display device with pin-array type tactile feedback and thermal feedback, in *Proceedings 2006 IEEE International Conference on Robotics and Automation, 2006. ICRA 2006.* (IEEE) (2006), pp. 3917–3922.
37. J. Pasquero, V. Hayward, STReSS: A practical tactile display system with one millimeter spatial resolution and 700 Hz refresh rate, in *Proc. Eurohaptics*, vol. 2003 (2003), pp. 94–110.
38. V. Hayward, J. M. Cruz-Hernández, Tactile display device using distributed lateral skin stretch, in *ASME international mechanical engineering congress and exposition* (American Society of Mechanical Engineers), vol. 26652 (2000), pp. 1309–1314.

39. Y. Ikei, K. Wakamatsu, S. Fukuda, Vibratory tactile display of image-based textures. *IEEE Computer Graphics and Applications* **17** (6), 53–61 (1997).
40. M. Etezad, R. Joshi, R. Alexander, F. L. Cibrian, 3D-Printed Models for Optimizing Tactile Braille & Shape Display. *IEEE Transactions on Haptics* (2024).
41. Z. A. Zook, A. M. Okamura, Y. Kamikawa, Effects of Latency and Refresh Rate on Force Perception via Sensory Substitution by Force-Controlled Skin Deformation Feedback, in *2018 IEEE International Conference on Robotics and Automation (ICRA)* (IEEE) (2018), pp. 506–511.
42. G. Frediani, F. Carpi, Tactile display of softness on fingertip. *Scientific reports* **10** (1), 20491 (2020).
43. Q. Zhang, S. Zhang, X. Zhu, T. Jiang, The Haptic Tele-operation System for Tactile Internet: Architecture, Challenges, and Implementation. *IEEE Network* (2025).
44. Y. Y. Lee, R.-H. Wu, S. T. Xu, Applications of linear Hall-effect sensors on angular measurement, in *2011 IEEE International Conference on Control Applications (CCA)* (2011), pp. 479–482, doi:10.1109/CCA.2011.6044465.
45. D. Leonardis, D. Chiaradia, G. Santamato, C. Camardella, A. Frisoli, Rendering Fine Tactile Feedback With a Novel Hydraulic Actuation Method for Wearable Haptic Devices. *IEEE Access* (2024).
46. H. Wang, S. Okamoto, Softness Perception Interfered by Friction in Gliding Virtual Surfaces. *IEEE Access* (2025).
47. L. Felicetti, *Analysis and rendering of contact vibrational stimuli for tactile perception*, Ph.D. thesis, INSA de Lyon; Università degli studi La Sapienza (Rome) (2024).
48. B. Camillieri, J. Faucheu, R. Ackerley, N. Le Moing, M.-A. Bueno, Influence of finger movement direction on friction-induced vibrations and perception of textured surfaces. *Tribology International* p. 110844 (2025).

49. A. M. Lund, Measuring usability with the use questionnaire¹². *Usability interface* **8** (2), 3–6 (2001).
50. J. Brooke, SUS: a retrospective. *Journal of usability studies* **8** (2) (2013).
51. J. R. Lewis, J. Sauro, Item benchmarks for the system usability scale. *Journal of Usability studies* **13** (3) (2018).
52. M. Alzoubi, S. Al-Hallaj, M. Abu-Ayyad, Modeling of compression curves of flexible polyurethane foam with variable density, chemical formulations and strain rates. *Journal of Solid Mechanics* **6** (1), 82–97 (2014).
53. K. Pakenaite, E. Kamperou, M. J. Proulx, A. Sharma, P. Hall, Pic2Tac: Creating Accessible Tactile Images using Semantic Information from Photographs, in *Proceedings of the Eighteenth International Conference on Tangible, Embedded, and Embodied Interaction* (2024), pp. 1–12.
54. L. Yang, *et al.*, Depth Anything V2 (2024), <https://arxiv.org/abs/2406.09414>.
55. A. Kirillov, *et al.*, Segment Anything (2023), <https://arxiv.org/abs/2304.02643>.

Supplementary materials

Tactile Display System Design and Fabrication

Theoretical Modeling and Control for Stiffness Rendering

Theoretical Justification for the Nonlinear Control Law

User Questionnaire Survey

Figs. S1 to S2

Tables S1 to S2

Movies S1 to S2

Supplementary Materials for
***ArrayTac*: A tactile display for simultaneous rendering of shape,**
stiffness and friction

Tianhai Liang, Shiyi Guo, Baiye Cheng, Zhengrong Xue, Han Zhang, Huazhe Xu*

*Corresponding author. Email: huazhe_xu@mail.tsinghua.edu.cn

This PDF file includes:

Tactile Display System Design and Fabrication

Theoretical Modeling and Control for Stiffness Rendering

Theoretical Justification for the Nonlinear Control Law

User Questionnaire Survey

Figs. S1 to S2

Tables S1 to S2

Captions for Movie S1 to S2

Other Supplementary Materials for this manuscript:

Movies S1 to S2

Supplementary materials

Tactile Display System Design and Fabrication

In this section, we provide a detailed description of the hardware design of ArrayTac, including component selection, fabrication, and assembly methods.

Actuator Array Design and Assembly The core of the display system is a 4×4 actuator array, which is composed of 16 independently addressable actuator units. The exploded view of this actuator array is shown in Fig. 7A. The output of each unit is transmitted via a bent steel wire (304 stainless steel, 1 mm diameter), converging onto a 6×6 mm square area at the tip. A single actuator unit, with dimensions of only $12.4 \times 8.4 \times 76$ mm, is primarily composed of a housing, a piezoelectric ceramic element, a three-stage amplification lever mechanism, a permanent magnet, a Hall effect sensor, and an end-effector wire. An external view of the fully assembled unit is shown in Fig. 1D, and an internal perspective view is provided in Fig. 1E.

The piezoelectric ceramic element (DCpiezo, DCS3-050536) drives the actuator's amplification mechanism. By applying a voltage, it can generate a micro-scale displacement of up to $40 \mu\text{m}$. This displacement is then amplified 125-fold by a novel three-stage micro-lever amplification mechanism, producing a maximum vertical travel of 5mm at the end of the final lever. The displacement is ultimately transmitted through the steel wire connected to this end lever. An axially magnetized, sintered NdFeB magnet (N35) is adhesively bonded onto the final-stage lever. The swing of the lever can be detected by a Hall effect sensor (Allegro, A1324) fixed to the top of the housing, which measures the change in the magnetic field, thereby enabling closed-loop position feedback. To prevent magnetic interference due to the close proximity of the units, the housing and levers are fabricated from AISI 1045 steel, which has good magnetic permeability and serves as an effective magnetic shield.

To ensure the consistency and accuracy of the amplification ratio across all units, each lever is designed as a solid body extruded from a closed two-dimensional profile. With the exception of the final-stage lever, the other levers in the amplification mechanism are identical (as shown in Fig. 1E). This design allows multiple linkages to be fabricated simultaneously using high-precision (± 0.005 mm) wire EDM, guaranteeing the uniformity of critical dimensions such as pivot points

and lever arm lengths. Additionally, miniature deep groove ball bearings (1 mm inner diameter \times 3 mm outer diameter \times 1 mm width) are used to reduce friction at the rotating shafts, further ensuring consistent resistance.

Beneath the piezoelectric element, a threaded fine-tuning mechanism is designed to allow for precise height adjustment of the piezoelectric ceramic element, compensating for inconsistencies arising from assembly errors, as shown in Fig. 1E. This mechanism consists of two main parts made from AISI 1045 steel: first, a movable base that supports the piezoelectric element and remains adjustable before being locked; and second, a threaded adjustment seat that is fixed to the housing with two bolts. The seat houses an M3 set screw that makes contact with the bottom surface of the movable base. Rotating this screw allows for fine adjustment of the movable base's height. After the desired adjustment is complete, the locking bolts on the movable base are tightened to ensure the stability and precision of the overall structure.

XYZ Sliding Platform Design and Assembly The system is mounted on an XYZ serial three-degree-of-freedom (3-DOF) zero-gravity sliding platform. The exploded view of the XYZ sliding platform is shown in Fig. 7B. This allows the operator to explore a larger virtual surface within a 60 \times 60 \times 185 mm (X-Y-Z) three-dimensional space, effectively extending the limitations of the physical workspace. To reduce operational resistance and ensure an immersive interactive experience, the XY plane is constructed with two pairs of orthogonally arranged linear guide rails (TGN5C) and sliders. The Z-axis is built with a pair of stainless steel Linear Shaft (D20 \times 320 mm) and linear bearings, achieving smooth, low-friction motion across all three axes. Both sides of the platform are equipped with constant force spring mechanisms that provide a nearly constant upward force in the Z-direction (a tension of 9.8 N per spring) at any height to balance the platform's self-weight. This provides the operator with a nearly weightless haptic feedback experience. The platform's linear displacement on the three axes is converted into rotational displacement by rack and pinion mechanisms (X and Y axes) and a synchronous belt mechanism (Z-axis), which is then measured by high-resolution rotary encoders (1024 PPR). This allows for the real-time detection and calculation of the platform's absolute coordinates in 3D space.

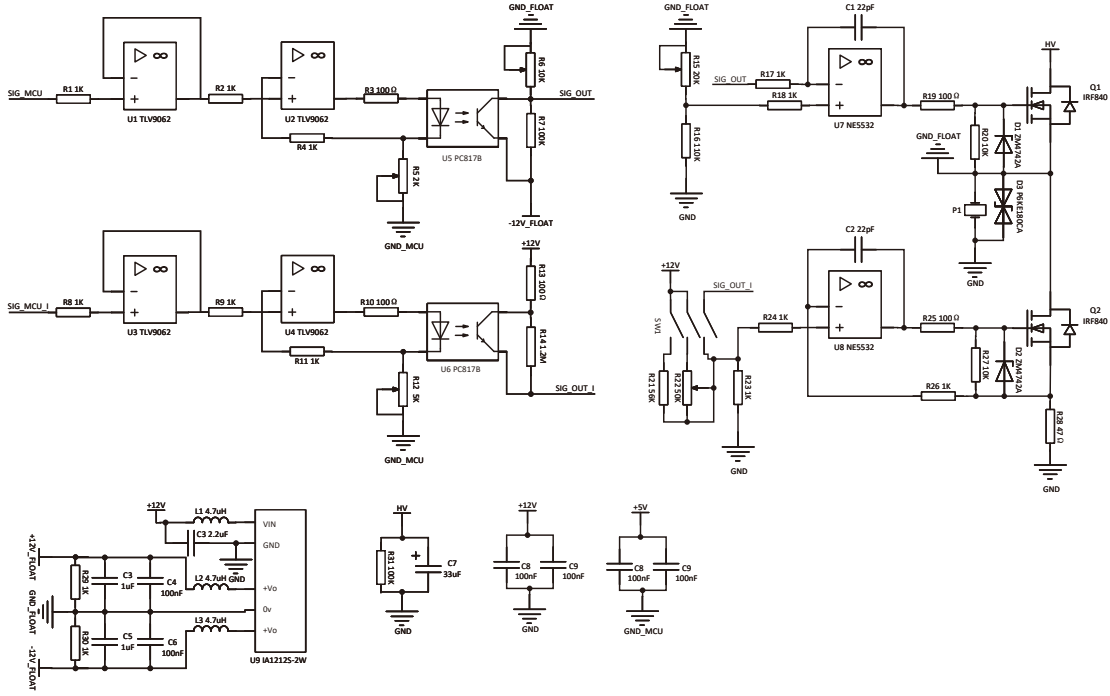


Figure S1: The schematic of the driver circuit.

Drive Circuits Design and Assembly We selected the STM32G431CBU6 microcontroller, manufactured by STMicroelectronics, as the control unit for each display element. This MCU features a Cortex-M4 core with a maximum clock frequency of 170 MHz, and includes an integrated DSP and FPU for efficient real-time computation. It is equipped with two DAC channels, two ADC modules, one FDCAN interface, and four UART interfaces, fully meeting the system’s control and communication requirements. To further expand the available analog output channels, we implemented a second-order RC low-pass filter to convert the 100 kHz base-frequency PWM signals generated by the MCU into smooth DC voltages, effectively enabling PWM-based DAC functionality. The RC filter parameters for the first and second stages were set to 3.9 k Ω , 10 nF, and 39 k Ω , 1 nF, respectively. For displacement sensing, we employed the A1324 linear Hall sensor produced by Allegro, which forms the core of the end-effector displacement measurement unit.

The power drive circuitry is illustrated in Fig. 7D. To charge the piezoelectric actuator, we used an operational amplifier configured with voltage-series negative feedback, while another operational amplifier was used to implement current-series negative feedback, creating a controllable constant-current source for actuator discharge. This design clamps the voltage across the piezoelectric

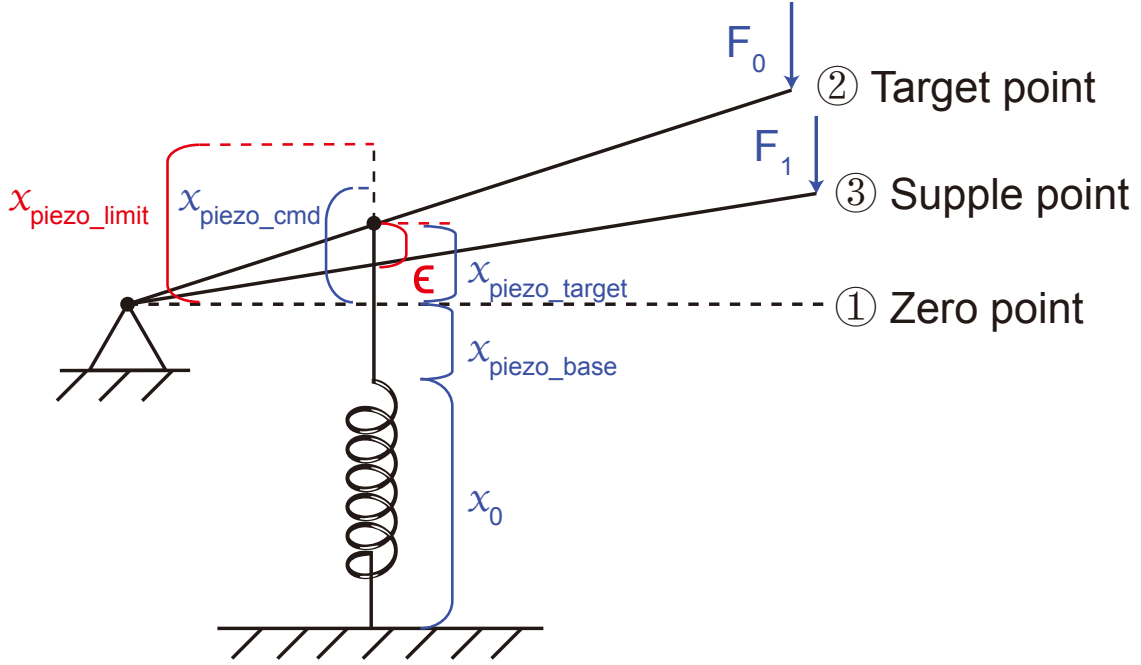


Figure S2: Physical principle schematic for stiffness rendering.

ceramic precisely to the target value. We selected TLV9062 (a low-cost rail-to-rail op-amp from TI) and NE5532 (an audio-grade op-amp) for signal conditioning, and IRF840 power MOSFETs for high-voltage switching.

To improve circuit safety and electrical isolation, we integrated IA1212S-2W isolated DC-DC converters to transform the 12 V supply into floating dual supplies, enabling isolated ground driving. PC817B optocouplers were used for high-low voltage signal isolation. All PCBs were designed with 4 layers and manually soldered and debugged during assembly.

Theoretical Modeling and Control for Stiffness Rendering

To achieve high-fidelity rendering of surface stiffness, we first established a physical model of the haptic actuator. From this model, we derived an expression for the system's equivalent stiffness, which forms the basis of the control strategy.

System Physical Model The core of the haptic actuator is a piezoelectric element that drives a multi-stage lever mechanism. To analyze its input-output relationship, we modeled this system, as shown in Fig. S2. The key physical variables are defined as follows: F_{piezo} is the driving force from

the piezoelectric element, x_0 is the natural length of the piezoelectric ceramic, $x_{\text{piezo_base}}$ refers to the baseline displacement required by the piezoelectric actuator to bring the unit to its zero (reference) position; F_{actuator} and x_{actuator} are the output force and displacement at the end-effector; and A is the lever's displacement amplification gain ($A > 1$). To render a specific surface geometry, the control system is given a target displacement for the actuator, $x_{\text{actuator_target}}$, so the piezoelectric element also has a target displacement, $x_{\text{piezo_target}}$. The deviation from this target, caused by external load, is denoted as ϵ and is measured in real-time by a Hall effect sensor. The element's actual displacement above its zero reference, x_{piezo} , is therefore given by $x_{\text{piezo}} = x_{\text{piezo_target}} - \epsilon$. To actuate the system, the control circuit generates a voltage corresponding to a commanded no-load displacement, denoted as $x_{\text{piezo_cmd}}$.

Based on the principle of work conservation for an ideal lever, the displacement and force relations are:

$$x_{\text{actuator_target}} = A \cdot x_{\text{piezo_target}} \quad (\text{S1})$$

$$x_{\text{actuator}} = A \cdot x_{\text{piezo}} = A \cdot (x_{\text{piezo_target}} - \epsilon) \quad (\text{S2})$$

$$F_{\text{actuator}} = \frac{F_{\text{piezo}}}{A} \quad (\text{S3})$$

The piezoelectric element itself acts as an elastic actuator. Its driving force, F_{piezo} , is proportional to the difference between the commanded displacement, $x_{\text{piezo_cmd}}$, and its actual measured displacement, x_{piezo} , under external load. Denoting the intrinsic stiffness of the piezoelectric element as K_{piezo} , its constitutive equation is:

$$F_{\text{piezo}} = K_{\text{piezo}}(x_{\text{piezo_cmd}} - x_{\text{piezo}}) = K_{\text{piezo}}(x_{\text{piezo_cmd}} - (x_{\text{piezo_target}} - \epsilon)) \quad (\text{S4})$$

Overview of the two-stage control process Fig. S2 illustrates the complete stiffness control process:

Number 1 means the system drives the piezoelectric actuator to extend by x_{base} , bringing the mechanism to its mechanical zero point.

Number 2 means the closed-loop control stage, a PID controller regulates the actuator extension to $x_{\text{piezo}} = x_{\text{piezo_target}}$, aligning the end-effector displacement with the desired target and entering

closed-loop control. As the external normal force F_0 gradually increases, the commanded displacement $X_{\text{piezo_cmd}}$ also increases, generating a reaction force $F_{\text{piezo}} = A \cdot F_0$ to counteract the applied load. During this stage, the steady-state error ϵ remains zero, and the end-effector displacement is maintained at the target position despite increasing F_0 . This corresponds to the high-stiffness behavior of region A in Fig. 8B and manifests as the y-intercept in the measured force-displacement curve Fig. 8D, which increases with the normalized stiffness parameters k .

Number 3 When F_0 reaches F_1 , $x_{\text{piezo_cmd}}$ hits the saturation threshold $x_{\text{piezo_limit}}$ defined in Fig. 8A. At this point, the system can no longer maintain zero error, resulting in $x_{\text{piezo}} < x_{\text{piezo_target}}$ and producing an error term ϵ . This error is then used to modulate $X_{\text{piezo_cmd}}$ through the designed feedforward penalty control strategy, enabling adaptive stiffness rendering and reproducing the nonlinear characteristics of region B in Fig. 8B.

The closed-loop control during the first stage is automatically governed by the PID controller. In the following parts, we demonstrate the effectiveness of the feedforward penalty control strategy.

Derivation and Control of Equivalent Stiffness The stiffness perceived by the user, termed the equivalent stiffness K_{eff} , is defined as the rate of change of the output force with respect to the magnitude of the end-effector's deformation. From Eq. (S2), the deformation from the target position is $A \cdot \epsilon$. Therefore, we define the equivalent stiffness as:

$$K_{\text{eff}} = \frac{dF_{\text{actuator}}}{d(A \cdot \epsilon)} = \frac{1}{A} \frac{dF_{\text{actuator}}}{d\epsilon} \quad (\text{S5})$$

To find the term $dF_{\text{actuator}}/d\epsilon$, we first establish the relationship between the output force and the sensor signal by combining Eqs. (S3) and (S4):

$$F_{\text{actuator}} = \frac{K_{\text{piezo}}}{A} (x_{\text{piezo_cmd}} - x_{\text{piezo_target}} + \epsilon) \quad (\text{S6})$$

Differentiating Eq. (S6) with respect to ϵ , and noting that $x_{\text{piezo_cmd}}$ is related to ϵ in our control system, we get:

$$\frac{dF_{\text{actuator}}}{d\epsilon} = \frac{K_{\text{piezo}}}{A} \left(\frac{dx_{\text{piezo_cmd}}}{d\epsilon} + 1 \right) \quad (\text{S7})$$

Finally, substituting this result back into our expression for K_{eff} yields:

$$K_{\text{eff}} = \frac{1}{A} \left[\frac{K_{\text{piezo}}}{A} \left(\frac{dx_{\text{piezo_cmd}}}{d\epsilon} + 1 \right) \right] = \frac{K_{\text{piezo}}}{A^2} \left(\frac{dx_{\text{piezo_cmd}}}{d\epsilon} + 1 \right) \quad (\text{S8})$$

Equation (S8) reveals the core principle enabling programmable stiffness rendering. The term $\frac{K_{\text{piezo}}}{A^2}$ represents the inherent passive stiffness of the actuator structure. The term $\frac{K_{\text{piezo}}}{A^2} \frac{dx_{\text{piezo_cmd}}}{d\epsilon}$ represents the active stiffness modulation provided by the controller. By implementing a specific algorithm in the microcontroller to precisely control the dynamic relationship between the command $x_{\text{piezo_cmd}}$ and the sensor feedback ϵ —that is, by setting the value of the derivative $\frac{dx_{\text{piezo_cmd}}}{d\epsilon}$ —we can actively control the overall equivalent stiffness K_{eff} perceived by the user.

Implementation of Nonlinear Stiffness Profile To emulate the characteristic biphasic force-displacement curves of soft materials, we implemented a specific nonlinear control law for the term $dx_{\text{piezo_cmd}}/d\epsilon$. The commanded displacement $x_{\text{piezo_cmd}}$ is actuated via the control voltage:

$$x_{\text{piezo_cmd}} = \beta \cdot (U_{\text{output}} - U_{\text{base}}), \quad (\text{S9})$$

where β denotes the voltage-to-displacement conversion coefficient of the piezoelectric ceramic, so $x_{\text{piezo_base}} = \beta \cdot U_{\text{base}}$, $x_{\text{piezo_limit}} = \beta \cdot (U_{\text{limit}} - U_{\text{base}})$.

Accordingly, the previously introduced control equation 2 can be rewritten as:

$$x_{\text{piezo_cmd}} = x_{\text{piezo_limit}} \cdot \left(1 - (1 - k) \cdot \frac{\epsilon}{x_{\text{piezo_limit}}} \right)^n, \quad (\text{S10})$$

which is calculated using a tunable penalty term with exponent n . We evaluated penalty terms of first, second, and third order ($n = 1, 2, 3$) to determine the optimal implementation. A linear penalty ($n = 1$) was found to adjust stiffness uniformly but failed to capture the nonlinear yielding behavior. Higher-order penalties ($n > 1$) introduced the desired nonlinearity, and simulations in Fig. 8C confirmed that their force-displacement curves match empirical data for materials like HR foam more closely. However, the third-order penalty ($n = 3$), while theoretically closer in some cases, introduced excessive nonlinearity that led to system instability and unpredictable haptic feedback during physical implementation. Therefore, a quadratic penalty ($n = 2$) was adopted as the optimal compromise, providing a realistic rendering of the material's yielding behavior while maintaining robust and stable system performance.

Theoretical Justification for the Nonlinear Control Law

In our results, we describe a control strategy for rendering nonlinear stiffness that employs a tunable penalty term with an exponent n . Here, we provide the theoretical justification for selecting

a quadratic penalty ($n = 2$) as the optimal implementation.

Physical Constraints for Realistic Stiffness Rendering The force-displacement curve of many real-world soft materials, such as HR foam, shows that the perceived stiffness is not constant but increases as the material is compressed. To realistically emulate this behavior, our control law must satisfy two physical constraints:

1. **Positive Stiffness:** The rendered object must always resist compression, meaning the equivalent stiffness must be positive ($K_{\text{eff}} > 0$).
2. **Increasing Stiffness:** The stiffness should increase as the deformation (ϵ) increases, meaning the rate of change of stiffness with respect to deformation must be positive ($dK_{\text{eff}}/d\epsilon > 0$).

Mathematical Formulation of Constraints From our physical model, the equivalent stiffness is given by:

$$K_{\text{eff}} = \frac{K_{\text{piezo}}}{A^2} \left(\frac{dx_{\text{piezo.cmd}}}{d\epsilon} + 1 \right) \quad (\text{S11})$$

Applying the two constraints to this equation yields the required mathematical conditions for our control law $x_{\text{piezo.cmd}}(\epsilon)$. Since K_{piezo}/A^2 is a positive constant, Constraint 1 ($K_{\text{eff}} > 0$) simplifies to:

$$\frac{dx_{\text{piezo.cmd}}}{d\epsilon} > -1 \quad (\text{S12})$$

For Constraint 2 ($dK_{\text{eff}}/d\epsilon > 0$), we differentiate Eq. (S11) with respect to ϵ :

$$\frac{dK_{\text{eff}}}{d\epsilon} = \frac{K_{\text{piezo}}}{A^2} \frac{d^2x_{\text{piezo.cmd}}}{d\epsilon^2} > 0 \quad (\text{S13})$$

This simplifies to the second condition:

$$\frac{d^2x_{\text{piezo.cmd}}}{d\epsilon^2} > 0 \quad (\text{S14})$$

Therefore, a valid control law must have a first derivative greater than -1 and a second derivative that is strictly positive over the operational range of ϵ .

Analysis of Penalty Term Exponents Our control law is defined by the relationship between the output voltage U_{output} and the commanded displacement $x_{\text{piezo_cmd}}$. From the forward, we know the commanded displacement is:

$$x_{\text{piezo_cmd}}(\epsilon) = x_{\text{piezo_limit}} \cdot \left(1 - \frac{1-k}{x_{\text{piezo_limit}}} \epsilon\right)^n, \quad (\text{S15})$$

where the $x_{\text{piezo_limit}} = \beta \cdot (U_{\text{limit}} - U_{\text{base}})$ represent the commanded displacement corresponding to the voltage limit.

The first and second derivatives of this function with respect to ϵ are:

$$\frac{dx_{\text{piezo_cmd}}}{d\epsilon} = -n(1-k) \left(1 - \frac{1-k}{x_{\text{piezo_limit}}} \epsilon\right)^{n-1} \quad (\text{S16})$$

$$\frac{d^2x_{\text{piezo_cmd}}}{d\epsilon^2} = n(n-1) \frac{(1-k)^2}{x_{\text{piezo_limit}}} \left(1 - \frac{1-k}{x_{\text{piezo_limit}}} \epsilon\right)^{n-2} \quad (\text{S17})$$

We now analyze this function for $n = 1, 2, 3$.

Case 1: Linear Penalty ($n = 1$) The equivalent stiffness at the end effector is given by:

$$K_{\text{eff}} = k \cdot \frac{K_{\text{piezo}}}{A^2} \quad (\text{S18})$$

This is an elegant result, showing that the stiffness can be linearly tuned by simply adjusting k . However, the second derivative is:

$$\frac{d^2x_{\text{piezo_cmd}}}{d\epsilon^2} = 0 \quad (\text{S19})$$

This violates Condition 2, as the stiffness does not increase with deformation.

Case 2: Quadratic Penalty ($n = 2$) The first derivative is:

$$\frac{dx_{\text{piezo_cmd}}}{d\epsilon} = -2(1-k) \left(1 - \frac{1-k}{x_{\text{piezo_limit}}} \epsilon\right) > 2k - 2 \quad (\text{S20})$$

The second derivative is:

$$\frac{d^2x_{\text{piezo_cmd}}}{d\epsilon^2} = \frac{2(1-k)^2}{x_{\text{piezo_limit}}} \quad (\text{S21})$$

Since all terms are positive, this is always greater than zero, satisfying Condition 2. It can be readily derived that when $k > 0.5$, condition 1 holds for all values of ϵ , which is consistent with the behavior shown in Fig. 8D.

Case 3: Cubic Penalty ($n = 3$) The first derivative is:

$$\frac{dx_{\text{piezo_cmd}}}{d\epsilon} = -3(1 - k) \left(1 - \frac{1 - k}{x_{\text{piezo_limit}}} \epsilon \right)^2 > 3k - 3 \quad (\text{S22})$$

It can be readily derived that when $k > 0.67$, condition 1 holds for all values of ϵ . However, the adjustable range of k becomes too narrow, and the system nonlinearity is excessively large, which compromises control stability. Therefore, this configuration is not adopted.

Conclusion Based on this analysis, the quadratic penalty ($n = 2$) is the lowest-order nonlinear term that satisfies both physical constraints: it provides a positive equivalent stiffness whose value correctly increases with deformation across the relevant operational range. This provides a clear theoretical justification for our selection of $n = 2$ for emulating nonlinear soft materials.

User Questionnaire Survey

To quantitatively assess system usability and user experience, 22 participants completed a modified version of the USE questionnaire—adapted to the experimental context—along with the standard System Usability Scale (SUS) after the main experiments. Table S1 and Table S2 present the detailed contents of the USE and SUS questionnaires, respectively.

Table S1: Usefulness, Satisfaction, and Ease of Use (USE) questionnaire items. This table lists the detailed contents of the USE questionnaire. The table lists all items grouped by their corresponding dimensions. Participants rated each item on a 7-point Likert scale (1 = strongly disagree, 7 = strongly agree; NA = not applicable).

Dimension	Item	Question (Item Content)
Usefulness	1.1	It helps me be more effective.
	1.2	It helps me be more productive.
	1.3	It is useful.

Continued on next page

Table S1 (continued) — Usefulness, Satisfaction, and Ease of Use (USE) Questionnaire Items (continued).

Dimension	Item	Question (Item Content)
	1.4	It makes the things I want to accomplish easier to get done.
	1.5	It saves me time when I use it.
	1.6	It meets my needs.
	1.7	It does everything I would expect it to do.
Ease of Use	2.1	It is easy to use.
	2.2	It is simple to use.
	2.3	It is user friendly.
	2.4	It requires the fewest steps possible to accomplish what I want to do with it.
	2.5	It is flexible.
	2.6	Using it is effortless.
	2.7	I can use it without written instructions.
	2.8	I don't notice any inconsistencies as I use it.
	2.9	Both occasional and regular users would like it.
	2.10	I can use it successfully every time.
Ease of Learning	3.1	I learned to use it quickly.
	3.2	I easily remember how to use it.
	3.3	It is easy to learn to use it.
	3.4	I quickly became skillful with it.
Satisfaction	4.1	I am satisfied with it.
	4.2	I would recommend it to a friend.
	4.3	It is fun to use.
	4.4	It works the way I want it to work.
	4.5	It is wonderful.

Continued on next page

Table S1 (continued) — Usefulness, Satisfaction, and Ease of Use (USE) Questionnaire Items (continued).

Dimension	Item	Question (Item Content)
	4.6	I feel I need to have it.
	4.7	It is pleasant to use.
Performance	5.1	I think the device distinguishes shapes effectively.
	5.2	I think the device distinguishes stiffness effectively.
	5.3	I think the device distinguishes friction effectively.
	5.4	I think the device allows me to clearly perceive desktop objects and their locations through touch.

Table S2: System Usability Scale (SUS) questionnaire items. This table lists the 10 items used in the SUS questionnaire. Each item represents a statement about the system, and participants indicate their level of agreement on a 5-point Likert scale.(1 = strongly disagree, 5 = strongly agree)

Item	Question (Item Content)
1	I think that I would like to use this system frequently.
2	I found the system unnecessarily complex.
3	I thought the system was easy to use.
4	I think that I would need the support of a technical person to be able to use this system.
5	I found the various functions in this system were well integrated.
6	I thought there was too much inconsistency in this system.
7	I would imagine that most people would learn to use this system very quickly.
8	I found the system very cumbersome to use.
9	I felt very confident using the system.
10	I needed to learn a lot of things before I could get going with this system.

Caption for Movie S1. Comprehensive demonstration of the ArrayTac system, rendering methods, and experimental applications. This video provides a comprehensive overview of ArrayTac, a tactile display capable of simultaneously rendering shape, stiffness, and friction. The video first presents the system’s core capabilities and application scenarios, and then introduces two main application frameworks: Tac-Anything, which directly extracts and renders multidimensional tactile semantics from images; and Tele-Touch, a simulated remote palpation system designed for tumor localization and diagnosis. The video also details the hardware and mechanical design of the individual actuator units and explains the fundamental principles of multidimensional tactile rendering, including shape, stiffness, and friction. It further presents extensive quantitative analysis results from volunteer experiments. Finally, the video reports the results of the USE and SUS questionnaires, demonstrating the system’s excellent overall usability and high user satisfaction.

Caption for Movie S2. Demonstration of remote palpation experiment using the ArrayTac tactile display. The video illustrates a teleoperation setup where a user in “City A” controls a robotic arm in “City B”, located 1,000 km away, to palpate a medical breast tumor phantom. The ArrayTac device provides real-time haptic feedback to the user. The “ArrayTac 4 × 4 Height” 3D bar chart displays the dynamic physical height (z-axis, in mm) of the device’s 4 × 4 actuator array. The “Combination Viewer” plots the 2D spatial coordinates (x and y axes) of the probe relative to a “Forbidden Area” and a working “Boundary”. At the end, the video presents a participant’s hand-drawn result, demonstrating the successful haptic identification and localization of “Malignant” and “Benign” tumors in the phantom.